

Studies of Nanoclusters' Collision
Depositions on a Crystalline Surface and Graphene, and Negative Restitution Coefficient of
Nanoclusters

Kuniyasu Saitoh

January 11, 2011

©Copyright by
Kuniyasu Saitoh
2011

Acknowledgments

I would like to acknowledge Prof. Hayakawa who is my supervisor of PhD course of science in Kyoto University. I am very grateful that he taught me many things about physics, research, and scientific mind. I really appreciate all the advice he gave me for writing this thesis. I also gratefully thank Prof. Wada and all members of Prof. Hayakawa's group for their fruitful advice and comments on research. I also thank all staffs of Yukawa institute for theoretical physics (YITP) and Division of Physics and Astronomy, Graduate School of Science, Kyoto University for their kindness and hospitality.

I am grateful to Prof. Luding, Prof. Kuninaka, Prof. Otsuki, Prof. Isobe, Prof. Hatano, and people in the granular material community for their help and fruitful discussion. I also would like to acknowledge Prof. Brilliantov and Dr. Bodrova for their collaboration on the part of this thesis and agreement to include the results in this thesis. I also thank the members of department of mathematics in University of Leicester for their hospitality, where the part of this thesis have been carried out. I would like to thank Prof. Paquette for his critical reading of a couple of our published papers.

Parts of the numerical computation in this work were carried out using computers of the YITP. My research was supported by (i) the Global COE program "The Next Generation of Physics, Spun from Universality and Emergence" from the Ministry of Education, Culture, Sports, Science and Technology (MEXT) of Japan and (ii) the Research Fellowship of the Japan Society for the Promotion of Science for Young Scientists (JSPS) and the Grant-in-Aid of MEXT (Grant No. 21.1958). In particular, I thank the bilateral international exchange program (BIEP) which enable me to stay at University of Leicester and collaborate with Prof. Brilliantov and Dr. Bodrova.

I am grateful to the YITP program, the Global COE program from MEXT, and the Society of Powder Technology, Japan for giving me the chance to organize the international workshop titled "Recent Progress in Physics of Dissipative Particles - *From fine powders to macroscopic behaviors of granular particles* -" which was held from November 24 to 26, 2010 at YITP and is strongly related to the part of results of this thesis.

Finally, I would like to thank my wife, Megumi, for her much support to my research and understanding of my life.

Curriculum Vitae

Education

- April 2008 - PhD student, Division of Physics and Astronomy, Graduate School of Science, Kyoto University
- March 2006 M. A. (Science), Kyoto University
- April 2004 - March 2006 Master course, Division of Physics and Astronomy, Graduate School of Science, Kyoto University
- March 2004 B. S. (Science), Kyoto University
- April 2000 - March 2004 Bachelor course, Faculty of Science, Kyoto University

Fellowship

- April 2009 - March 2011 Research Fellow of the Japan Society for the Promotion of Science (DC2)
- November 2009 - December 2009 Visiting research, Department of Mathematics, University of Leicester

Work Experience

- April 2006 - March 2008 Employee, DeNA Co., Ltd.

Publications

1. Kuniyasu Saitoh, Anna Bodrova, Hisao Hayakawa, and Nikolai V. Brilliantov,
"Negative Normal Restitution Coefficient Found in Simulation of Nanocluster Collisions",
Phys. Rev. Lett. **105**, 238001 (2010) featured as Editors' Suggestion.
2. Kuniyasu Saitoh and Hisao Hayakawa,
"Motion of a free-standing graphene sheet induced by the collision with an argon nanocluster:
Analyses of the detection and heat-up of the graphene",
Phys. Rev. **B 81**, 115447 (2010).
3. Kuniyasu Saitoh and Hisao Hayakawa,
"Simulation of depositions of a Lennard-Jones cluster on a crystalline surface",
Prog. Theor. Phys. **122**, 1081 (2009).
4. Kuniyasu Saitoh and Hisao Hayakawa,
"Rheology of a granular gas under a plane shear",
Phys. Rev. **E 75**, 021302 (2007).

Abstract

In this thesis, we show the results of the molecular dynamics (MD) simulations of the collisions between nanoscale objects such as (i) nanocluster depositions on a crystalline surface, (ii) nanocluster depositions on a free-standing graphene, and (iii) oblique impacts of two nanoclusters. The aim of this thesis is to analyze the mechanics of nanoscale objects and to explain the results of the molecular dynamics simulations in terms of the continuum mechanics.

At first, depositions of amorphous Lennard-Jones nanocluster on a crystalline surface are numerically investigated. From the results of the MD simulation, we found that the deposited nanocluster exhibits a transition from multilayered adsorption to monolayered adsorption at a critical incident speed. Employing the energy conservation law, we estimate the incident speed at which evaporation occurs during the impact. We demonstrate the estimated value well agrees with the results of the MD simulation. We also explain that the scaled adsorption parameter $\eta \equiv N_{adh}/N_{cls}$, where N_{adh} and N_{cls} are the number of atoms adsorbed on the substrate and the cluster size, respectively, is proportional to the square of the incident speed. The boundary shape of the adsorbed nanocluster depends strongly on the incident speed, and some unstable modes grow during the impact. We also analyze the wettability between different Lennard-Jones atoms, and temperature dependence of a deposited nanoclusters.

At second, the motion of a free-standing graphene induced by nanocluster impact is investigated. The graphene is bended by the incident nanocluster and a transverse deflection wave is observed. We find that the time evolution of the deflection is semi-quantitatively described by the elastic beam theory. The time evolution of the temperature profile of graphene is also measured, and we demonstrate that the analysis based on the least dissipation principle well explains the result in the early stage of impact.

At third, the oblique impacts of nanoclusters are studied by the MD simulation and theoretically. In the MD simulations, we explore two models – Lennard-Jones clusters and particles with covalently bonded atoms. In contrast to the case of macroscopic bodies, the standard definition of the normal restitution coefficient yields negative values for oblique collisions of nanoclusters. We explain this effect and propose a proper definition of the restitution coefficient which is always positive. We develop a theory of an oblique impact based on continuum model of particles. A good agreement between the macroscopic theory and simulations leads to the conclusion that macroscopic concepts of elasticity, bulk viscosity and surface tension remain valid for nanoparticles of a few hundred atoms.

Contents

1	Introduction	8
1.1	Nanoscience and nanotechnology	8
1.2	Nanocluster	8
1.3	Argon nanocluster	10
1.4	Silicon nanocluster	10
1.5	Nanocluster deposition on a surface	10
1.6	Collision of two nanoclusters	11
1.7	Charge-up of nanocluster	12
1.8	Mechanics of graphene and carbon nanotube	12
1.9	Quantum effect and the method of empirical potential	12
1.10	The aim of this thesis	13
1.11	Organization of this thesis	13
2	Depositions of a Lennard-Jones nanocluster on a crystalline surface	14
2.1	Introduction	15
2.2	Molecular dynamics simulation	16
2.2.1	Model	16
2.2.2	Setup	17
2.2.3	Numerical analysis of temperature dependence	18
2.3	Results	18
2.3.1	Time evolution of impacts	18
2.3.2	Incident speed dependences of the scaled cluster size and cluster adsorption parameter	20
2.3.3	Transition from partial wetting to perfect wetting of the deposited cluster	22
2.3.4	Morphology of the final configuration of the adsorbed atoms in the cluster	23
2.3.5	Wettability between different Lennard-Jones atoms	24
2.3.6	Temperature dependence of a deposited Lennard-Jones nanocluster	24
2.4	Discussion and conclusions	27
3	Depositions of an argon nanocluster on a free-standing graphene sheet	28
3.1	Introduction	29
3.2	Molecular dynamics simulation of the impact	29
3.3	Results	30
3.3.1	Time evolution of the deflection	30
3.3.2	Analysis of the deflection	31
3.3.3	Analysis of the heat-up	33
3.4	Discussion	35
3.5	Conclusion	35

4	Negative normal restitution coefficient for nanocluster collisions	36
4.1	Introduction	37
4.2	MD simulations	37
4.3	Modified definition of e	40
4.4	Theory of an oblique impact	41
4.5	Conclusion	43
5	Summary	45
A	Tersoff potential	46
A.1	Explicit form of the Tersoff potential	46
A.2	Forces between interacting three atoms	47
B	Brenner potential	50
B.1	Explicit form of the Brenner potential	50
B.2	Forces between interacting three atoms	51
C	Spin effect on the restitution coefficient of nanocluster	53
C.1	<i>Spin-less</i> approximation	53
C.2	Angular displacement α	54
C.3	Derivations of Eqs.(4.4), (4.5) and (4.13)	55
C.4	Spin effect on the restitution coefficient	55
D	Elastic modulus and surface tension of a nanocluster	57
D.1	Elastic modulus	57
	D.1.1 Isotropic compression	57
	D.1.2 Shearing deformation	58
D.2	Surface tension	58
	D.2.1 Model of interacting two spheres	58
	D.2.2 Model of compressed two spheres	60

Chapter 1

Introduction

1.1 Nanoscience and nanotechnology

In the last decade, science and technology of nanomaterials are explosively developed [1–3]. The purpose of nanoscience and nanotechnology is to control nanoscale objects in order to innovate nanoscale devices. Because the nanoscale objects are intermediate between single atoms and macroscopic materials, the properties of nanoscale objects are often peculiar [4] and many researchers investigate such peculiar aspects of nanoscale objects, i.e. nanoclusters, graphene sheets, carbon nanotubes, etc.

1.2 Nanocluster

Nanocluster is an aggregate containing $10 - 10^6$ atoms which are bonded by the interatomic forces [5–7]. If the total charge of nanocluster is neutral, the nanocluster is called *neutral nanocluster*. For example, argon nanocluster is a typical neutral nanocluster, in which argon atoms are bonded by the van der Waals interactions [8, 9]. On the other hand, gold nanocluster, in which constituent gold atoms are bonded by metallic bonds and free electrons play an important role, is one of the most studied metallic nanocluster [10–13]. Because nanoclusters are categorized by the species of atom and the interatomic interaction [14–17], and each aspect of nanocluster is extremely different, we restrict ourselves to the study of neutral nanoclusters such as argon nanocluster and silicon nanocluster. Therefore, the effect of charge, which we describe in Sec.1.7, is ignored in this thesis.

The equilibrium states of neutral nanocluster are characterized by temperature and size [18–31]. Figure 1.1 exhibits the phase diagram of the Lennard-Jones nanocluster reprinted from Ref. [25]. In the case of extremely low temperature, we can see face centered cubic (FCC), decahedral, and icosahedral structures. On the other hand, if the temperature is relatively high, we can see "liquid" nanocluster in spite of size [22, 25, 32]. Because the number of atoms in nanocluster is 10^6 at most, the finite size effect plays an important role in the physics of nanoclusters. For example, thermal fluctuation of each atom can influence the structure of nanocluster, and negative thermal capacity and smooth jump of heat capacity (Fig.1.2) are found in the melting of nanoclusters [32–36]. The number of atoms on surface of nanocluster is equally matched for the number of atoms inside the nanocluster. Therefore, nanocluster has an extremely high reactivity and the van der Waals force is most important to the interaction between two neutral nanoclusters [5, 7].

In experiment, nanoclusters are made by cooling down a supersaturated vapor [6, 37–39]. There are essentially two ways to cool down the supersaturated vapor: (i) employing an adiabatic expansion through a nozzle into a high vacuum region, or (ii) mixing with a cold rare gas flow. Nanoclusters can also be made by hitting a material with a laser pulse or an ion beam.

The nanoclusters produced in laboratory are detected by diffraction of electron beam [6, 37–39]. In this method, the fast electrons are scattered from the nanocluster and the diffraction rings around

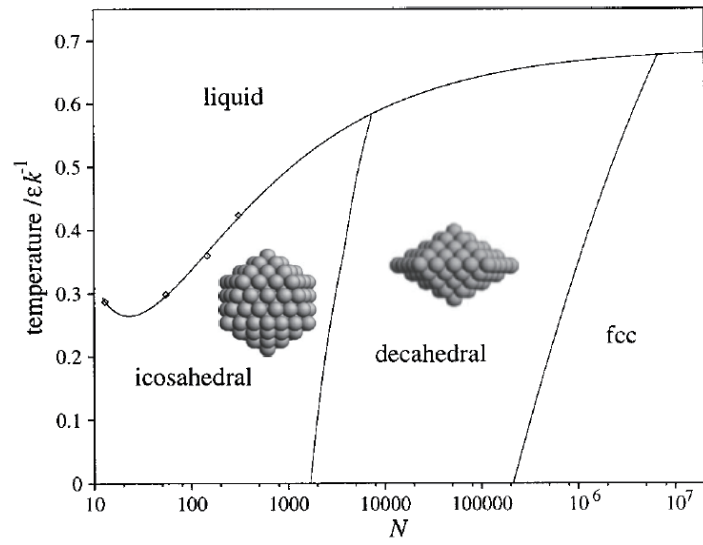


Figure 1.1: Phase diagram of the Lennard-Jones nanocluster reprinted from Ref. [25].

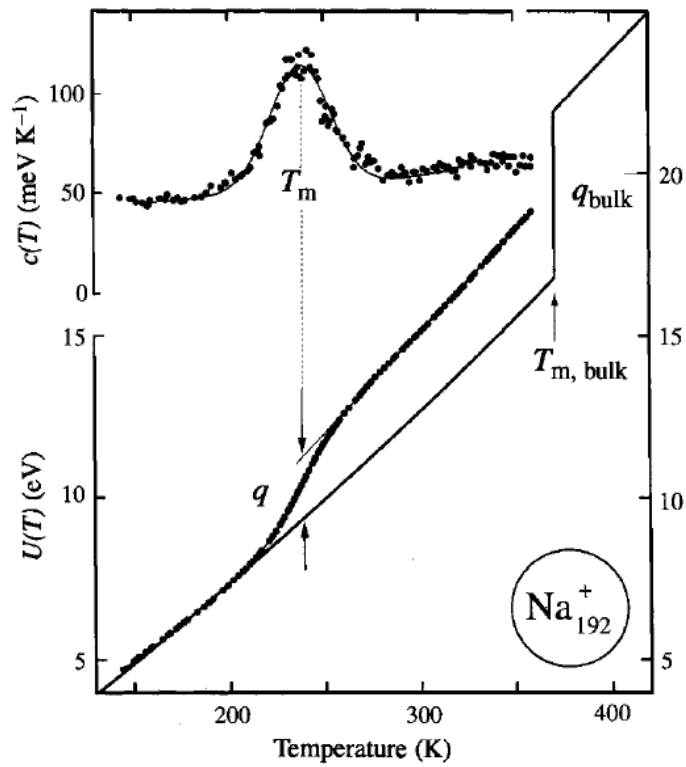


Figure 1.2: Heat capacity $c(T)$ and the caloric curve $U(T)$ of a positively charged sodium nanocluster containing 192 atoms (Ref. [35]).

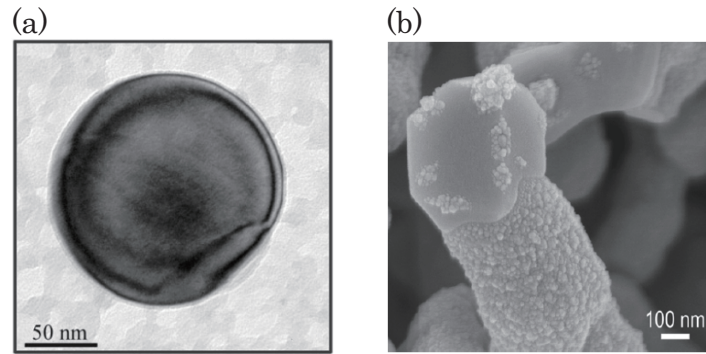


Figure 1.3: (a) A bright-field TEM micrograph of an 80nm radius Si nanosphere (Ref. [48]). (b) SEM image of nanoparticle-coated silicon on a substrate (Ref. [49]).

the primary position of the electron beam is recorded. The interpretation of the diffraction profiles is not straightforward, however, the size, structure, and temperature of nanoclusters can be detected by this method.

1.3 Argon nanocluster

Argon nanocluster is one of the most studied nanoclusters and has been investigated experimentally and numerically since the early 1980s [8, 9]. Because argon is a rare gas, it is a typical neutral nanocluster. The equilibrium state of argon nanocluster depends on the size and temperature, and the FCC, decahedral, and icosahedral structures are possible in the low temperature regime [22, 25, 32]. However, the glassy state of argon nanocluster, i.e. *amorphous argon nanocluster*, was found in the electron diffraction experiment [40], and this result triggered many numerical simulations of amorphous Lennard-Jones nanocluster [41–45]. From the results of this experiment, the amorphous argon nanocluster is stable if the number of argon atoms is up to $N = 800$, however, if the number of argon atoms becomes larger, the structure is changed to the multilayered icosahedron [40].

1.4 Silicon nanocluster

Silicon nanocluster is one of the most important nanocluster for practical purpose because of the intense photoluminescence at room temperature [46–49]. There are many experiments to produce neutral silicon nanoclusters by hitting a laser pulse to a bulk silicon. Silicon nanoclusters can also be produced by injecting vapor-phase silicon into an hydrogenated thermal plasma [49]. In this case, the surfaces of silicon nanoclusters, which are deposited on a substrate, are hydrogenated, and it is expected that the surfaces of silicon nanoclusters are coated by hydrogen atoms during the free flight. Figure 1.3 shows (a) a TEM image of an Si nanocluster [48] and (b) a SEM image of nanoparticle-coated silicon nanocluster deposited on a substrate [49]. From the results of experiments and numerical simulations, it is known that silicon nanocluster changes its shape from prolate structure to spherical diamond structure around the number of constituent atoms $N = 20$ [46].

1.5 Nanocluster deposition on a surface

It is highly important to investigate the behavior of nanocluster depositions on a substrate for fabrication of high-quality films used in nanoscale electronic devices and photonic devices [50]. The ionized cluster beam (ICB) technique makes it possible to control the translational kinetic energy of nanoclus-

ter [51–53]. Therefore, there have been many experimental and theoretical studies of nanocluster depositions on a substrate [54–61].

The outcome of nanocluster deposition is mainly influenced by the incident speed of nanocluster [54, 55]. If the incident speed is extremely high, the cratering or implantation of the substrate is observed [62–68]. On the other hand, if the incident speed is low enough, nanocluster is adsorbed or rebounded on the substrate [69–72]. In this thesis, the incident speed is relatively low (0.01eV at most), and the adsorption state of deposited nanocluster is mainly analyzed.

1.6 Collision of two nanoclusters

Collisions of two spherical particles are one of the most fundamental problem in physics, and it is also important in chemistry, engineering, and many other fields [73–77]. The pioneering paper "On the contact of elastic solids" in 1882 by Hertz [78] analyzed contact mechanics of elastic bodies and proposed the Hertzian distribution of contact pressure which acts on the contact area between colliding two macroscopic spheres. Because the origin of the Hertzian contact pressure is only elasticity, contact forces caused by the other effects, for example, the surface energy and viscoelasticity of macroscopic spheres, are investigated by many researchers [79, 80]. Especially, the JKR theory for the adhesive forces is well known [81], and it is applied to many fields of granular physics, astrophysics, etc.

Although there are much effort to understand the normal head-on collisions, the role of the tangential forces parallel to the contact plane during oblique collisions are not well understood. Indeed, the process is affected by the stick and slip motion, the rolling frictions and the effect of roughness of particle's surface, and the mechanism of the oblique impact has not been well explained theoretically [79, 80].

Inelastic collisions, where a part of mechanical energy of colliding bodies transforms into heat, are common in nature and industry. Avalanches, rapid granular flows of sand, powders or cereals may be mentioned as pertinent examples [82, 83]. Moreover, inelastic collisions play an important role in astrophysical objects, like planetary rings, dust clouds, etc. An important characteristic of such collisions is the normal restitution coefficient e . The concept of a restitution coefficient, as a basic one of the classical mechanics, has been introduced long ago by Newton; it addresses an impact of macroscopic bodies. According to a standard definition, it is equal to the ratio of the normal component of the rebound speed, \mathbf{g}' (prime states for the post-collision value), and the impact speed, \mathbf{g}

$$e = -\frac{\mathbf{g}' \cdot \mathbf{n}}{\mathbf{g} \cdot \mathbf{n}}. \quad (1.1)$$

The unit inter-center vector $\mathbf{n} = \mathbf{r}_{12}/|\mathbf{r}_{12}|$ at the *collision instant* ($\mathbf{r}_{12} = \mathbf{r}_1 - \mathbf{r}_2$) specifies the impact geometry. Since particles bounce in the direction, opposite to that of the impact, e is positive, $e > 0$, and since the energy is lost in collisions, e is smaller than one, that is, $0 \leq e \leq 1$. This is a common statement in the majority of mechanical textbook, where it is also claimed that e is a material constant. Recent experimental and theoretical studies show, however, that the concept of a restitution coefficient is more complicated: First, it depends on an impact speed [84–87], second, it can exceed unity for a special case of oblique collisions with elastoplastic plate [88–90], where the energy of normal motion can increase at the expense of the energy of tangential motion [88–90].

The increasing interest to nanoparticles, inspired by its industrial significance, raises an important question, to what extent the macroscopic concepts are applicable and whether they acquire new features at a nanoscale. The collisions of nanoclusters has been studied in detail numerically [72, 91–95]. It was observed that the surface effects, due to the direct inter-cluster van der Waals interactions, play a crucial role: The majority of collisions of homogeneous clusters, built of the same atoms, lead to a fusion of particles [91, 92]; they do not fuse for high impact speeds, but disintegrate into pieces [91, 92]. This complicates the analysis of restitutive collisions, which may be more easily performed for particles with a reduced adhesion. Among possible examples of such particles are clusters of covalently

bonded atoms, especially when their surface is coated by atom of different sort, as for H- passivated Si nanospheres [72]. These particles can rebound from a substrate, keeping their form after an impact unaltered [72]. The bouncing nanoclusters demonstrate a surprising effect – the normal restitution coefficient can exceed unity even for strictly head-on collisions [93].

1.7 Charge-up of nanocluster

The effect of charges in ionized nanocluster is also an important issue of experimental and theoretical studies of nanocluster. Recent experimental technique of the FLASH free electron laser (FEL) is able to ionize nanocluster by photo-absorption of atoms in nanocluster [96]. Because the energy of the electron beam is much higher than the ionization potential (21.564eV, 8.152eV, and 13.598eV for an argon atom, a silicon atom, and a hydrogen atom respectively), the nanocluster is charged up during the irradiation process, and finally the Coulomb explosion occurs.

It is also possible to charge up nanoclusters by a collision. In this case, the kinetic energy of incident nanoclusters must be higher than the ionization potential of atoms in nanocluster. In this thesis, the incident speed of nanocluster is set on a low value (0.01eV at most), thus the effect of charge-up is neglected. However, the influence of ionization on collision dynamics is highly important as a future work.

1.8 Mechanics of graphene and carbon nanotube

Graphene is a two-dimensional atomic layer of carbon atoms packed into a honeycomb lattice. Because graphene can be wrapped up into fullerenes and rolled into carbon nanotubes, graphene is the most fundamental nanoscale carbon material and such flexibility of graphene encourages many researchers to investigate its mechanical properties [97–101]. Because graphene is a monolayer of carbon atoms, its thickness can not be defined precisely in the sense of the continuum mechanics. Therefore, the bending modulus

$$D = \frac{dM}{dk} \sim Yh^3, \quad (1.2)$$

where M , κ , Y , and h are the bending moment, the bending curvature, Young's modulus, and the thickness of graphene, respectively, can not be defined precisely, too. However, the bending modulus D can be measured experimentally by atomic force microscope (AFM) indentation, and different physical origins of D have been sought in experiments and numerical simulations [102–107]. There are essentially two ways to define the thickness h of graphene: (i) $h = 0.34\text{nm}$, which is the distance between two carbon layers in graphite, and (ii) $h \ll 0.34\text{nm}$, which is an effective thickness mainly proposed by the numerical simulations. Although there is an ambiguity in the definition of h , graphene is thought to be an extremely rigid plate with $Y = 1 \sim 3\text{TPa}$.

Carbon nanotube, on the other hand, is a quasi-one dimensional tube of carbon atoms. Many experimental and numerical studies have clarified the super rigidity of carbon nanotube [108–111], and it is a promising candidate for the next generation rigid fibers.

1.9 Quantum effect and the method of empirical potential

There are several methods for the numerical study of nanocluster. Thus, the choice of an appropriate one depends on the size of nanocluster, the time scale, and the situation.

In the case that nanocluster contains only a few atoms, for example the number of atoms in nanocluster is in the range of $2 \leq N \leq 10$, the first principle calculation, i.e. *ab initio* calculation of quantum mechanics or Hartree-Fock method, is used to take into account the quantum effects [112].

In this method, all electron calculations are possible [113], however, this method becomes cumbersome for larger size nanoclusters and the long time calculations are almost impossible.

The method based on density-functional theory [114–117] and quantum Monte Carlo simulation [118,119] can be accurate calculations, if the correlation terms, which is treated under approximations, are adequately calculated. Although the accuracy of approximations depends on the systems, these methods can deal with one hundred atoms by the semi-quantum approach.

In the case that the number of atoms is larger and the time scale is longer, classical interaction potentials, which are based on approximate quantum models, are necessary. These interaction potentials, i.e. *empirical potentials*, contain parameters fitted by experimental results or the first principle calculations. For example, the Lennard-Jones potential, which is a popular model for rare gases, contains the short-range repulsive part arisen from the wave function overlap between interacting two atoms, and the long-range attractive part arisen from the electric dipole polarization of two atoms (the London dispersion force).

In this thesis, because the number of atoms in nanocluster is ranged between a few hundreds and a few thousands, the classical molecular dynamics simulations with empirical potentials are adopted. Because we also use the Tersoff potential [120–125] and the Brenner potential [126–129] for the calculations of carbon and silicon atoms, respectively, the details of them are described in Appendix A and B.

1.10 The aim of this thesis

In this thesis, we show the results of the MD simulations of the collisions between nanoscale objects such as (i) nanocluster depositions on a crystalline surface, (ii) nanocluster depositions on a free-standing graphene, and (iii) oblique impacts of two nanoclusters. The aim of this thesis is to analyze the mechanics of nanoscale objects with the help of the continuum model to explain the results of the molecular dynamics simulations.

1.11 Organization of this thesis

This thesis is organized as follows: In Chapter 2, nanocluster depositions on a crystalline surface are numerically investigated. To clarify the adsorption state of deposited nanocluster, the critical incident speed, at which the deposited nanocluster forms a monolayer, is investigated. From the analysis based on the energy conservation law, the critical incident speed is estimated. In addition, the boundary shapes of adsorbed nanocluster are analyzed. We also analyze the influence of the interaction between different species of atoms and temperature dependence of deposited nanoclusters [130]. In Chapter 3, nanocluster depositions on a free-standing graphene sheet are investigated. The deflection waves propagating in the graphene sheet are observed, and the dynamic motion of the graphene is analyzed. Employing the linear theory for elastic plate, the time development of the deflection wave is reproduced in the early stage of the impact. An anisotropic temperature profile of the graphene is also observed, and such a profile is quantitatively explained by the least dissipation principle for an irreversible process [131]. In Chapter 4, oblique impacts of two nanoclusters are investigated. Because of the reorientation of the contact surface and the finite contact time, the conventional restitution coefficient becomes negative when the incident angle is large enough. The modified form of the restitution coefficient is introduced, which is always positive, and the macroscopic model for dissipative particles well reproduces the results of the MD simulations [132]. In Chapter 5, all the results and conclusions are summarized.

Chapter 2

Depositions of a Lennard-Jones nanocluster on a crystalline surface

2.1 Introduction

A nanocluster containing 10 – 10,000 molecules exhibits intermediate properties between bulk materials and individual molecules. Recently, there has been growing interest in the physics of nanoclusters. [4–7, 32] In particular, it is important to investigate the depositions of nanoclusters on solid surfaces for the construction of high-quality films used in nanoscale electronic devices and photonic devices. [50]

The ionized cluster beam (ICB) technique was developed by Yamada et al. [51, 52] The ICB technique is used to produce atomic clusters by employing adiabatic expansion of condensed vapour through a nozzle into a high-vacuum region. In the ICB technique, clusters are ionized by electron impact and then accelerated toward a substrate. Because the ICB technique controls the translational kinetic energy of the cluster, there have been many experimental and theoretical studies aimed at understanding the effect of the incident velocities of the cluster on the outcome of impact. [59–61]

The outcome of such a cluster impact is largely affected by the incident velocity, as seen from the phase diagrams in Refs. [54, 55] If the translational kinetic energy per atom becomes too large, the cluster can damage the substrate, and the cluster can break into pieces after the impact. [62–68] However, if the translational kinetic energy per atom is less than 100 eV, the cluster is adsorbed on the surface or reflected by the surface. Awasthi et al. carried out molecular dynamics simulations for collisions of Lennard-Jones clusters with weakly attractive surfaces. [70, 71] They discovered that the cluster rebounds when the translational kinetic energy of the cluster is larger than the adhesion energy. Moreover, they clarified that a transition from adhesion to rebound occurs at the critical translational kinetic energy. Järvi et al. carried out molecular dynamics simulations of low-energy deposition of individual metal clusters on a (100) surface. [69] They revealed that the heat generated by the impact partially or completely melts the deposited cluster. As a consequence, the atoms in the cluster are rearranged and adjusted to the atomic structure of the substrate. They found the maximum size at which single clusters align epitaxially on the substrate.

Recently, Kuninaka and Hayakawa have carried out molecular dynamics simulations of two identical colliding clusters and investigated impact phenomena of nanoclusters subject to thermal fluctuations. [93] They found super-rebound events in which the restitution coefficient is larger than 1. They confirmed the validity of the macroscopic quasi-static theory of cohesive collisions. [86] This suggests that the research on nanoclusters is relevant even for the study for fine powders whose diameters range from 100 nm to 1 μm . [73, 74] They also revealed the mechanism responsible for the super-rebound process, the normal rebound, and the merging.

Although early numerical studies assumed that the clusters are highly crystallised, we also need to know the properties of amorphous clusters. Indeed, it is easy to form metastable amorphous clusters in terms of the quench process from high-temperature liquids. [41–45, 133]

The main purpose of our paper is to understand the behavior of the deposited amorphous Lennard-Jones clusters on the crystalline surface at zero temperature. Here, we report on our molecular dynamics simulation of the depositions with the small incident energies per atom, which lie in the so-called soft-landing regime (0 – 2 eV). In addition, we report on the wettability between different Lennard-Jones atoms.

From the analysis of the final configurations of the deposited clusters, we find the existence of a morphological phase transition from the hemi-spherical droplet to the monolayer film at the critical incident speed. The multilayered adsorption state is described on the basis of the energy conservation law. Furthermore, we find that there are some unstable modes of the boundary shape of the deposited cluster.

This paper is organized as follows. Section 2 consists of three sections. In §2.1, we explain the model of our numerical simulation. We explain our setup of cluster depositions in §2.2. In §2.3, we explain how to analyze temperature dependence of deposited clusters numerically. Section 3 consists of five sections. In §3.1, we show some time evolutions of impact processes. In §3.2, we explain

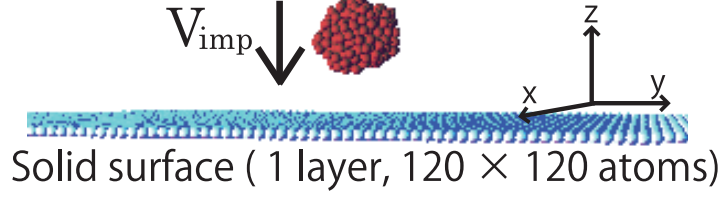


Figure 2.1: A snapshot of our simulation of a nanocluster deposition. The incident cluster contains 300 atoms that are bounded by the Lennard-Jones potential. The substrate consists of a single layer (120×120) of atoms on a triangular lattice.

how the cluster size and cluster adsorption parameter depend on the incident speed after the impact. In §3.3, we discuss the transition from partial wetting to perfect wetting of deposited clusters. In §3.4, we explain the morphological change of the final configuration of adsorbed atoms in clusters. In §3.5, we discuss the wettability between different Lennard-Jones atoms. In §3.6, we analyze the temperature dependence of deposited Lennard-Jones nanoclusters on a crystalline surface. In §4, we discuss our numerical results and summarize the conclusion.

2.2 Molecular dynamics simulation

2.2.1 Model

To investigate the nanocluster depositions on a substrate, we perform a molecular dynamics simulation. Figure 2.1 displays a snapshot of our numerical simulation. Because we are interested in neutral nanoclusters and substrates, the electrostatic interaction between atoms is not considered. We assume that the potential energy of the interaction between two atoms can be described using the Lennard-Jones (LJ) potential:

$$U(r_{ij}) = 4\epsilon_{\alpha\beta} \left\{ \left(\frac{\sigma_{\alpha\beta}}{r_{ij}} \right)^{12} - \left(\frac{\sigma_{\alpha\beta}}{r_{ij}} \right)^6 \right\}, \quad (2.1)$$

where subscripts α and β specify the species of LJ atoms and r_{ij} is the distance between two atoms labeled by i and j . Here, $\epsilon_{\alpha\beta}$ and $\sigma_{\alpha\beta}$ are, respectively, the strength of the interaction and diameter of the repulsive core between α and β atoms. If $\alpha \neq \beta$, we adopt the cross parameters of the LJ potential using the Lorentz-Berthelot rule as

$$\sigma_{\alpha\beta} = \frac{(\sigma_{\alpha} + \sigma_{\beta})}{2}, \quad \epsilon_{\alpha\beta} = \sqrt{\epsilon_{\alpha}\epsilon_{\beta}}. \quad (2.2)$$

We mainly investigate the case that the cluster and substrate are constructed using the same atoms, A. Here, we borrow the values of LJ parameters and mass of a typical inert gas, argon. Therefore, ϵ_{AA} , σ_{AA} , and the mass of an A atom m_A are 1.65×10^{-21} J, 3.405 \AA , and 6.63×10^{-26} kg, respectively. [134–136] On the other hand, to study the effect of the interaction energy between different atoms of the cluster and substrate, we introduce a C atom as the constituent of the substrate in §3.5. We use the values of LJ parameters and mass of carbon to the C atom, in which ϵ_{CC} , σ_{CC} , and the mass of C atom m_C are 3.86×10^{-22} J, 3.354 \AA , and 1.99×10^{-26} kg, respectively. [134–136] We should note that the interaction energy between the cluster and substrate, ϵ_{AC} , is several times weaker than ϵ_{AA} . In the following, we omit the subscripts of the LJ parameters of the interaction between the A atoms and we adopt simplified notations ϵ , σ . We also adopt m as the mass of an A atom. We use ϵ , σ , and m as the units of energy, length, and mass, respectively. Thus, the unit time is given by $\tau = \sqrt{m\sigma^2/\epsilon}$.

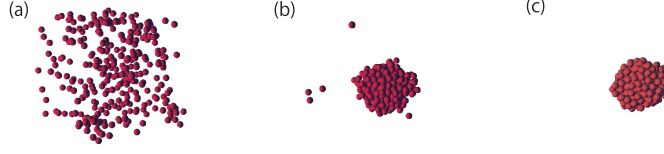


Figure 2.2: Illustration of an LJ cluster formation consisting of 300 A atoms. (a) Initial configuration of atoms in the gas phase at $T = 1.0\epsilon$. (b) A liquid cluster obtained from the quench into $T = 0.5\epsilon$. (c) An amorphous cluster obtained from the quench into $T = 0.01\epsilon$.

We use a single-layer surface, which involves 120×120 atoms on a triangular lattice as the substrate with the periodic boundary condition. [137, 138] We set the lattice constant to $2^{1/6}\sigma_{\alpha\alpha}$ ($\alpha = A, C$) as the equilibrium distance between atoms. To avoid the destruction of the substrate, each atom of the substrate is also tethered to its equilibrium position by an elastic spring. In actual impacts of nanoclusters on substrates, the energy induced by an impact is relaxed to the internal motion of the atoms of the bulk region of the substrate. To represent such energy relaxation, we simply introduce the viscous force proportional to its velocity. The introduction of the viscous force has another advantage to reduce the unrealistic boundary effects. Indeed, if we do not introduce the viscous force, the acoustic wave would be transmitted across the boundary. The atom of the substrate at \mathbf{r}_i satisfies the equation of motion

$$m_\alpha \frac{d^2 \mathbf{r}_i}{dt^2} = - \sum_j \frac{d}{d\mathbf{r}_i} U(r_{ij}) - k(\mathbf{r}_i - \mathbf{r}_i^{\text{eq}}) - \lambda \frac{d\mathbf{r}_i}{dt}, \quad (2.3)$$

where \sum_j is a summation over the interacting pairs i and j , and \mathbf{r}_i^{eq} is its equilibrium position, and m_α ($\alpha = A, C$) is the mass of an atom of the substrate. Because we consider the substrate as a rigid surface, we use the spring constant $k = 1.0 \times 10^3 \epsilon / \sigma^2$. We simply adopt the value $\lambda = 1.0 \sqrt{m\epsilon} / \sigma$ for the coefficient of viscosity.

We adopt the velocity Verlet method for numerical integration of the equation of motion for each atom with the time step $dt = 1.0 \times 10^{-3} \sqrt{m\sigma^2 / \epsilon}$. To reduce computational costs, we introduce the cutoff length $\sigma_{\text{cut}} = 3.0\sigma$ to the LJ potential, and we adopt the periodic boundary conditions in the horizontal xy directions and the free boundary condition in the vertical z direction. It should be noted that the viscous force is evaluated as the value at the previous time step for the numerical integration of Eq. (2.3).

2.2.2 Setup

We make an LJ cluster by the temperature quench [139] into the metastable phase of LJ fluid. [140] We prepare 32, 108, 255, 300, 500, and 862 atoms in a periodic box and equilibrate at the temperature $T = 1.0\epsilon$ with the number density $0.05\sigma^{-3}$ in the gas state (Fig. 2.2(a)). It should be noted that the unit of the temperature becomes ϵ , because we set the Boltzmann constant to be unity. To equilibrate the gas at a specific temperature, we perform the velocity scaling until $\tau = 2000\sigma \sqrt{m/\epsilon}$ for the relaxation to a local equilibrium state. We have confirmed the equilibration of the total energy in the initial relaxation process, and we quench the gas to $T = 0.5\epsilon$. After an equilibration, a weakly bounded liquid cluster is formed (Fig. 2.2(b)) and is quenched to $T = 0.01\epsilon$ to make it rigid. This two-step quenching is adopted to form one cluster from an initial gas state. Indeed, if we quench the system into $T = 0.01\epsilon$ directly, many small clusters appear. After this equilibration, we obtain an amorphous cluster (Fig. 2.2(c)). We place the amorphous cluster at 10σ above the substrate and give the cluster the translational velocity V_{imp} to make it collide against the substrate. It should be noted that the

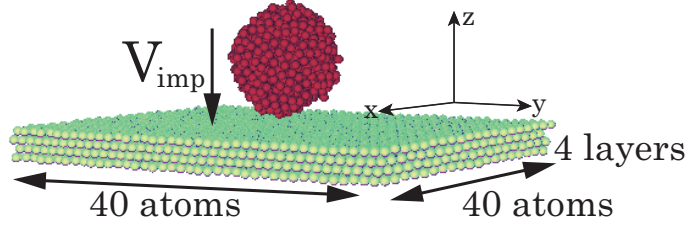


Figure 2.3: (Color online) A snapshot of our simulation of a deposition of a Lennard-Jones cluster. The incident cluster contains 862 atoms which are bounded by the Lennard-Jones potential. The substrate is a (111)-terminated fcc surface consists of 4 layers of 40×40 triangular lattice of atoms.

amorphous cluster is metastable to maintain its shape within our observation time. The incident angle of the cluster to the substrate normal is zero. The incident speed of the cluster ranges from $V_{\text{imp}} = 0.1$ to $5.0 \sqrt{\epsilon/m}$.

2.2.3 Numerical analysis of temperature dependence

To analyze temperature dependence of deposited nanoclusters, we use a (111)-terminated fcc crystalline surface for the substrate. Figure 2.3 shows the setup of numerical simulation. The (111)-terminated fcc surface consists of 4 layers of 40×40 triangular lattice. We set the lattice constant to $2^{1/6} \sigma_{\text{CC}}$. To avoid the destruction of the substrate, each atom of the substrate is tethered to its equilibrium position by an elastic spring. Thus the atom of the substrate at \mathbf{r}_i satisfies the equation of motion

$$m_C \frac{d^2 \mathbf{r}_i}{dt^2} = - \sum_j \frac{d}{d\mathbf{r}_i} U(r_{ij}) - k(\mathbf{r}_i - \mathbf{r}_i^{\text{eq}}), \quad (2.4)$$

where \sum_j is a summation over the interacting pairs i and j , and \mathbf{r}_i^{eq} is its equilibrium position. Because we consider the substrate as a rigid surface, we use the spring constant $k = 1.0 \times 10^2 \epsilon/\sigma^2$. We adopt the velocity scaling method every 0.5τ to equilibrate the substrate at a specific temperature. The temperature of the substrate is ranged from $T = 0.01\epsilon$ to 0.4ϵ . We adopt the periodic boundary conditions in the horizontal xy directions and the free boundary condition in the vertical z direction.

2.3 Results

2.3.1 Time evolution of impacts

Figures 2.4 and 2.5 display the time evolutions of the impact of the LJ cluster of 300 atoms on the crystalline surface. Figures 2.4(a)–(d) represent the case of $V_{\text{imp}} = 2.0 \sqrt{\epsilon/m}$, and Figs. 2.5(a)–(d) are the case of $V_{\text{imp}} = 4.0 \sqrt{\epsilon/m}$.

The incident cluster moves toward the substrate with its translational speed V_{imp} (Figs. 2.4(a) and 2.5(a)), and hits the substrate (Figs. 2.4(b) and 2.5(b)). After the hit, the cluster is only deformed to be a hemi-sphere (Fig. 2.4(c)) for the small incident speed. If the incident speed is, however, larger than a critical value, the deposited cluster is split into many pieces (Fig. 2.5(c)). After the impact, the deposited cluster is adsorbed on the substrate and settles into the final configuration (Figs. 2.4(d) and 2.5(d)).

We observe that the impact process and final configuration depend strongly on the incident speed V_{imp} . In the case of $V_{\text{imp}} < 1.7 \sqrt{\epsilon/m}$, no atoms can escape from the cluster during the impact. By contrast, some atoms evaporate during the impact process for $V_{\text{imp}} \geq 1.7 \sqrt{\epsilon/m}$. If the incident speed is relatively low, the final configuration is a hemi-sphere on the substrate, as in the case of a partial wetting of a liquid droplet on a dry surface. The deformation becomes larger as the incident speed

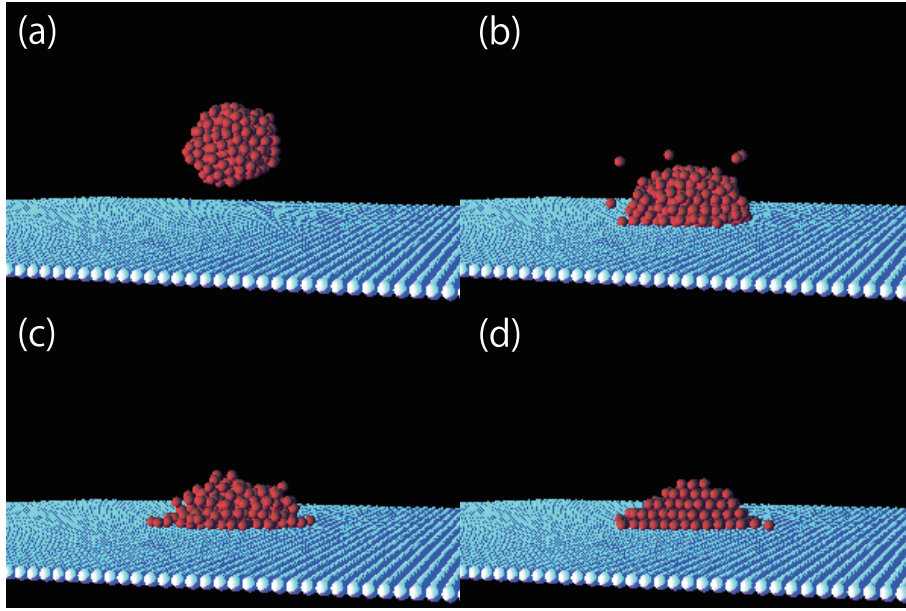


Figure 2.4: Time evolution of an impact of an LJ cluster of 300 atoms on the substrate, where the incident speed is $V_{\text{imp}} = 2.0 \sqrt{\epsilon/m}$. See the text for details.

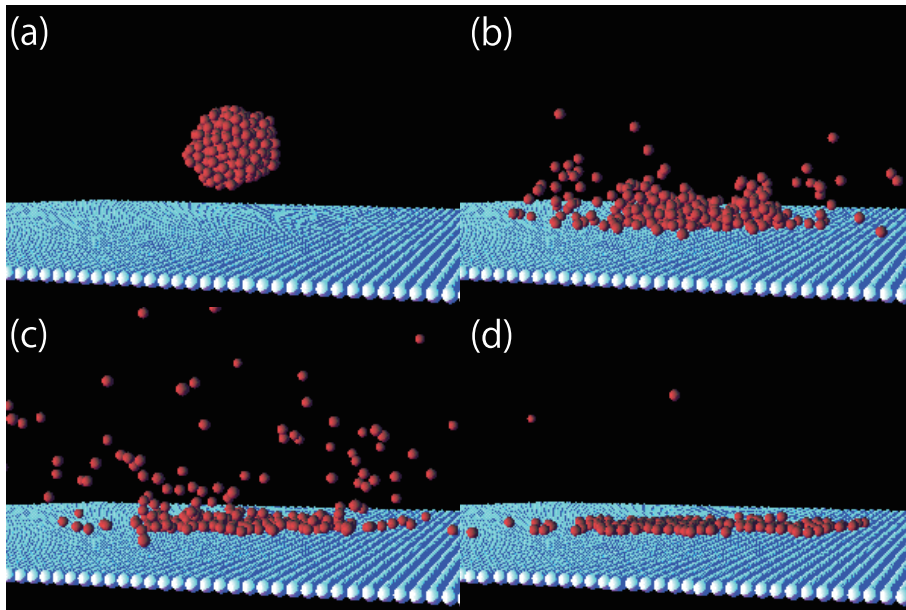


Figure 2.5: Time evolution of an impact of an LJ cluster of 300 atoms on the substrate, where the incident speed is $V_{\text{imp}} = 4.0 \sqrt{\epsilon/m}$. See the text for details.

increases. Above $V_{\text{imp}} = 3.3 \sqrt{\epsilon/m}$, the deposited cluster is completely split into fragments, and the absorbed atoms on the substrate form a monolayer coverage. Above $V_{\text{imp}} = 4.5 \sqrt{\epsilon/m}$, the deposited cluster bursts into fragments, and the absorbed coverage is no longer characterized by one cluster.

At the moment of impact, the temperature of the deposited cluster increases because the initial kinetic energy is transformed into internal motion. Then, the temperature decreases owing to the heat conduction into the bulk region of the material through the contact area. [69, 141, 142] The configuration of the deposited cluster is changed into an energetically favorable position during cooling. Furthermore, the atomic structure of the deposited cluster is adjusted to the substrate. Finally, the

configuration is frozen because of the loss of heat.

2.3.2 Incident speed dependences of the scaled cluster size and cluster adsorption parameter

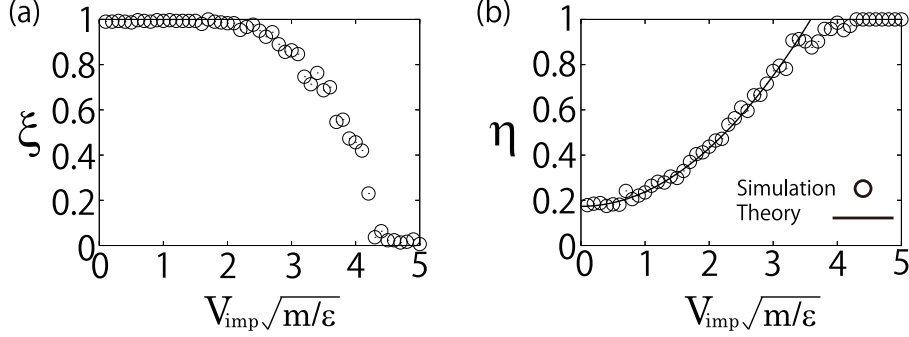


Figure 2.6: (a) A plot of the scaled cluster size ξ and (b) a plot of the cluster adsorption parameter η as functions of the incident speed for the cluster of 300 atoms.

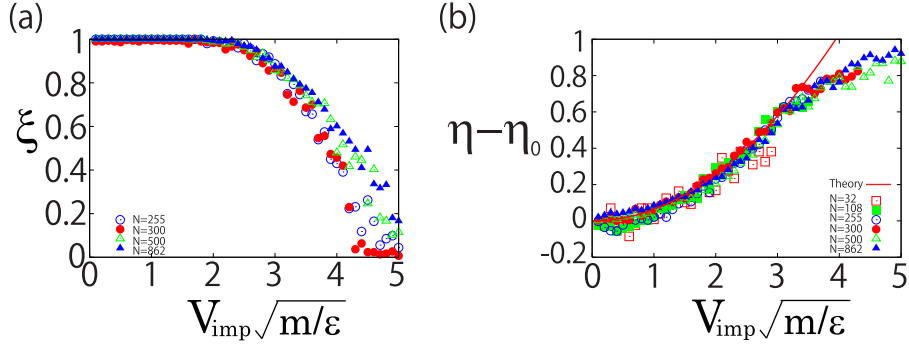


Figure 2.7: (a) Plot of the scaled cluster size ξ and (b) plot of the scaled cluster adsorption parameter η as functions of the incident speed.

In our simulation, the main cluster is detected using the clustering algorithm. [143] Following Allen and Tildesley, we adopt the critical atom separation $r_C = 1.6\sigma$. After the cluster settles into the final configuration, we represent N_{cls} as the number of atoms in the cluster. With the number of atoms in the cluster before the impact N , we introduce the scaled cluster size:

$$\xi \equiv \frac{N_{\text{cls}}}{N}. \quad (2.5)$$

If $\xi = 1$, no atoms can escape from the cluster after the impact. On the other hand, if $\xi < 1$, some atoms evaporate during the cluster impact.

Let us define an adsorbed atom in the cluster if an atom at \mathbf{r} in the cluster satisfies the relation $|\mathbf{r} - \mathbf{r}_s| < r_C$, where \mathbf{r}_s is the position of its nearest neighbor constituent of the substrate. Using the number of these adsorbed atoms N_{adh} , we can introduce the cluster adsorption parameter:

$$\eta \equiv \frac{N_{\text{adh}}}{N_{\text{cls}}}. \quad (2.6)$$

If $\eta < 1$, the cluster is regarded as a multilayered adsorption. However, if $\eta = 1$, the deposited cluster is perfectly spread on the substrate, and it is a monolayered adsorption.

Figures 2.6(a) and (b) plot the incident speed dependences of ξ and η for the cluster of 300 atoms. We find that ξ equals 1 below $V_{\text{imp}} = 1.7\sqrt{\epsilon/m}$, but it decreases above $V_{\text{imp}} = 1.7\sqrt{\epsilon/m}$. On the other hand, η increases with the incident velocity below $V_{\text{imp}} = 3.3\sqrt{\epsilon/m}$, but it is satisfied to $\eta \simeq 1$ above $V_{\text{imp}} = 3.3\sqrt{\epsilon/m}$. Figure 2.7(a) plots several results on ξ for $N = 255, 300, 500$, and 862 , while Fig. 2.7(b) is $\eta - \eta_0$ for $N = 32, 108, 255, 300, 500$, and 862 , where η_0 is η at $V_{\text{imp}} = 0$. It seems that $\eta - \eta_0$ is independent of the size of clusters, while ξ exhibits weak size dependence.

How can we understand the behaviors in Figs. 2.6 and 2.7? During the impact, the temperature in the cluster increases because the kinetic energy is transformed into internal motion. [69] We assume that the energy flux to the substrate Φ_{bulk} during the impact is small, and the temperature becomes maximum T_{max} when the speed of the center of mass of the cluster becomes zero. Thus, the energy conservation law can be written as

$$\frac{1}{2}mNV_{\text{imp}}^2 + \frac{3}{2}NT_0 \simeq \frac{3}{2}NT_{\text{max}} + \Delta S, \quad (2.7)$$

where T_0 is the temperature of the cluster before the impact, and ΔS is the change in the surface energy. With the introduction of the surface tension γ , the height of the deposited cluster h , the contact radius of the deposited cluster R , and the ratio $\phi = h/R$, ΔS is given by

$$\Delta S = \gamma(2\pi\phi R^2 - 4\pi R_0^2), \quad (2.8)$$

where R_0 is the mean radius of the cluster before the impact. By introducing the mean area fraction of the contact area $\rho_{\text{adh}} = N_{\text{adh}}/\pi R^2$, ΔS can be rewritten as

$$\Delta S = \gamma \left(\frac{2N_{\text{adh}}}{\rho_{\text{adh}}} - 4\pi R_0^2 \right). \quad (2.9)$$

From Eq. (2.7), T_{max} satisfies

$$T_{\text{max}} = T_0 + \frac{m}{3}V_{\text{imp}}^2 - \frac{2\Delta S}{3N}. \quad (2.10)$$

Because the binding energy per atom in the cluster is roughly equal to ϵ , the evaporation takes place at $T_{\text{max}} \simeq \epsilon$. In our simulation, T_0 is much smaller than T_{max} , and the last term on the right-hand side of Eq. (2.10) is negligible for large N . Thus, the evaporation is considered to take place near $V_{\text{imp}} \simeq \sqrt{3\epsilon/m}$. In Figs. 2.6(a) and 2.7(a), the scaled cluster size becomes $\xi < 1$ above $V_{\text{imp}} = 1.7\sqrt{\epsilon/m}$, which is consistent with the above estimation. For the clusters with 32 and 108 atoms, ξ decreases faster than the other cases. In such cases, we cannot ignore the last term on the right-hand side of Eq. (2.10).

During the impact, an evaporated atom carries away the volume energy u_V , which is the potential energy per atom and the kinetic energy $\frac{3}{2}T_{\text{max}}$ from the cluster. We assume that the internal energy of the deposited cluster decreases because of the energy flux to the bulk of the substrate. Therefore, after the cluster settles into the final configuration, the energy conservation law can be written as

$$\frac{1}{2}mNV_{\text{imp}}^2 + \frac{3}{2}NT_0 = \Delta S + \Phi_{\text{bulk}} + (1 - \xi)N\bar{E}, \quad (2.11)$$

where $\bar{E} = \frac{3}{2}T_{\text{max}} - u_V$ is the energy carried away by an evaporated atom. Here, $(1 - \xi)N$ represents the number of evaporated atoms. If the incident kinetic energy is not large, the number of atoms in the cluster is approximately preserved during the impact. Therefore, it is reasonable that the scaled cluster size satisfies $\xi \simeq 1$. If we assume $\phi \simeq 1$, the energy conservation law (Eq. (2.11)) can be simplified as

$$\eta = \frac{m\rho_{\text{adh}}}{4\gamma}V_{\text{imp}}^2 + \frac{\rho_{\text{adh}}}{2\gamma} \left(\frac{4\pi\gamma R_0^2}{N} - \frac{\Phi_{\text{bulk}}}{N} + \frac{3}{2}T_0 \right), \quad (2.12)$$

where we have used Eqs. (2.6) and (2.9).

We use $\rho_{\text{adh}} = 0.91$, because the adsorbed atoms should match the hexagonal lattice on the substrate. The mean radius R_0 of a cluster consisting of N atoms satisfies $R_0 = r_0 N^{1/3}$, where we use $r_0 = 0.68\sigma$ as a fitting parameter. The solid line in Fig. 2.6(b) is the theoretical prediction (Eq. (2.12)), where the surface tension $\gamma \simeq 3.5\epsilon/\sigma^2$ and the energy flux per atom $\varphi_{\text{bulk}} = \Phi_{\text{bulk}}/N \simeq 1.7\epsilon$ are the two other fitting parameters.

The second term on the right-hand side of Eq. (2.12) can be written as

$$\eta_0(N) = \frac{\rho_{\text{adh}}}{2\gamma} \left(4\pi r_0^2 \gamma N^{-1/3} - \varphi_{\text{bulk}} + \frac{3}{2} T_0 \right). \quad (2.13)$$

It is interesting that $\eta - \eta_0(N)$ is independent of the cluster size. Figure 2.7(b) plots our numerical results $\eta - \eta_0(N)$ for $\eta < 1$, which support the validity of the theoretical prediction (solid line).

2.3.3 Transition from partial wetting to perfect wetting of the deposited cluster

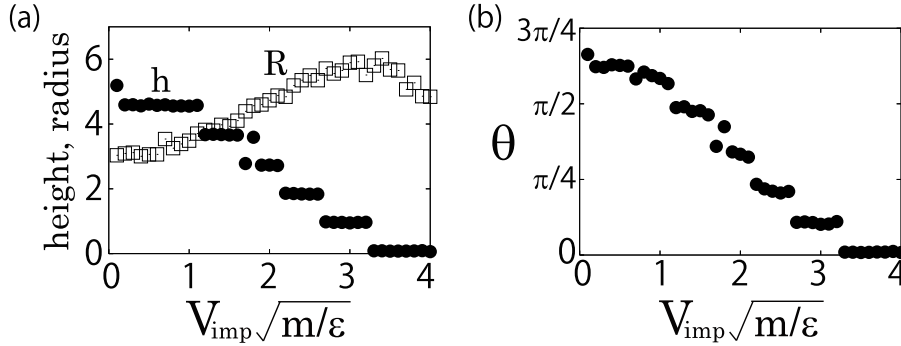


Figure 2.8: (a) Plots of the height h (filled circle) and contact radius R (open square) and (b) a plot of the contact angle θ as functions of the incident speed for the LJ cluster of 300 atoms.

Let us introduce the radius of the equimolar dividing surface (Gibbs Surface) [143]

$$R^2 = -\frac{1}{\rho_{\text{adh}}} \int_0^\infty \frac{d\rho(r)}{dr} r^2 dr \quad (2.14)$$

as the contact radius of a deposited cluster, where $\rho(r)$ is the area fraction of the contact area with radial distance from the center of mass of the adsorbed atoms in the cluster. We also define the cluster height h as $z_{\text{max}} - z_0$, where z_{max} is the maximum vertical position in the atoms in the cluster, and z_0 is the minimum vertical position. Assuming a meniscus shape to the deposited cluster, we geometrically calculate the contact angle θ .

Figure 2.8 displays h , R , and θ for the deposited cluster consisting of 300 atoms as functions of the incident speed. We observe that the cluster height h decreases and the contact radius R increases as the incident speed increases. Above $V_{\text{imp}} = 3.3 \sqrt{\epsilon/m}$, the height and contact angle become zero, which implies that the deposited cluster becomes a monolayer film and is perfectly wetting on the substrate. In this regime, the monolayer film is spread further and its boundary is partially chipped. Therefore, the contact radius decreases. The clusters consisting of 108, 255, 500, and 864 atoms are also perfectly wetting on the substrate at critical incident velocities. However, it should be noted that the transition from multilayer film to monolayer film is only the morphological change of the deposited cluster. In the case of the cluster consisting of 32 atoms, the number of adsorbed atoms is too few to define the wetting parameters h , R , and θ .

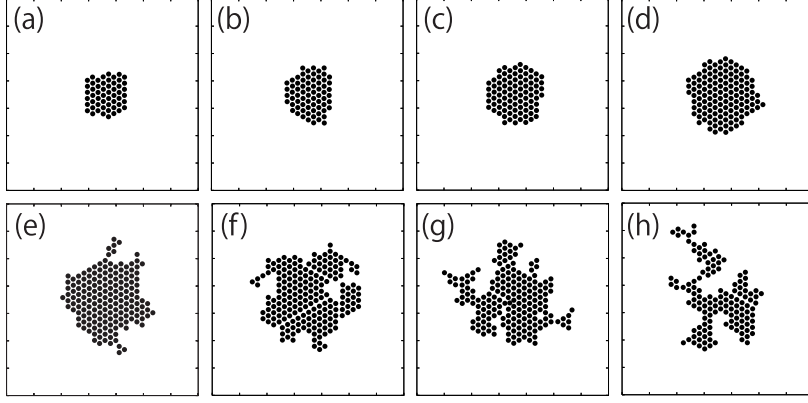


Figure 2.9: Configurations of the adsorbed atoms in a deposited cluster of 300 atoms for each incident speed. V_{imp} equals (a) 0.5, (b) 1.0, (c) 1.5, (d) 2.0, (e) 2.5, (f) 3.0, (g) 3.5, and (h) $4.0 \sqrt{\epsilon/m}$.

2.3.4 Morphology of the final configuration of the adsorbed atoms in the cluster

The boundary shape of the contact area depends strongly on the incident speed. To investigate the morphology of the boundary shape, we define the radial distance of the boundary $r = f(\psi)$. Here, r and ψ are the usual radial and azimuthal coordinates. We take the origin to the center of mass of the adsorbed atoms in the cluster. Moreover, we define a dimensionless variable $g(\psi)$ for the boundary [144] as

$$g(\psi) = \frac{f(\psi) - R}{R}. \quad (2.15)$$

We also use its Fourier representations $g(\psi) = \sum_n g_n e^{in\psi}$, with the integer $n = 0, \pm 1, \pm 2, \dots$.

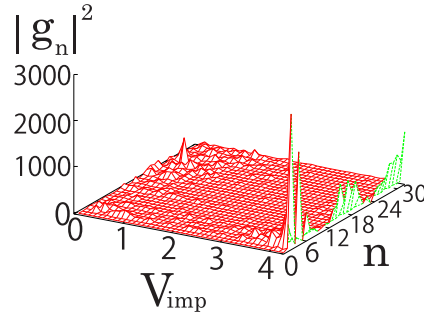


Figure 2.10: Three dimensional plot of $|g_n|^2$ of a deposited cluster of 300 atoms as the function of the incident speed and the mode n .

Figures 2.9(a)–(h) are the variety of the final horizontal configurations of the adsorbed atoms in the cluster consisting of 300 atoms, and Fig.2.10 exhibits the variation in $|g_n|^2$ for each incident speed and the mode n . We find that there are three phases in the boundary shape. Below $V_{\text{imp}} = 1.5 \sqrt{\epsilon/m}$, the boundary shape is grainy (Figs. 2.9(a), (b)), and $|g_n|^2$ has some peaks at higher modes. This may be caused by the small number of adsorbed atoms. In the case of $1.5 \sqrt{\epsilon/m} < V_{\text{imp}} < 3.0 \sqrt{\epsilon/m}$, the deposited cluster is uniformly spread on the substrate (Figs. 2.9(c), (d), (e), (f)). Thus, peaks of $|g_n|^2$ vanish and their boundaries can be fitted by circles. In the case of $3.0 \sqrt{\epsilon/m} < V_{\text{imp}} < 4.0 \sqrt{\epsilon/m}$, the deposited cluster becomes a thin film or a monolayer film. In this regime, the boundary is partially chipped (Figs. 2.9(g), (h)), where $|g_n|^2$ has intense peaks at some modes in our simulation. Above $V_{\text{imp}} = 4.0 \sqrt{\epsilon/m}$, the deposited cluster bursts into fragments and the number of adsorbed atoms is too few to define R . Thus, we cannot define $g(\psi)$ in this regime.

The thermal fluctuation of a circular geometry step is estimated as $\langle |g_n|^2 \rangle = T/2\pi\beta Rn^2$ from the equipartition of energy among the g_n . [144, 145] Here, β is the step edge stiffness. In our simulation, the thermal fluctuation is estimated as $\langle |g_n|^2 \rangle \sim 0.1$, while the $|g_n|^2$ has peaks ranging from 1000 to 3000 above $V_{\text{imp}} = 3.0 \sqrt{\epsilon/m}$. Therefore, these intensive peaks reflect on the growth of some unstable modes of g_n during the spread of the deposited cluster on the substrate.

2.3.5 Wettability between different Lennard-Jones atoms

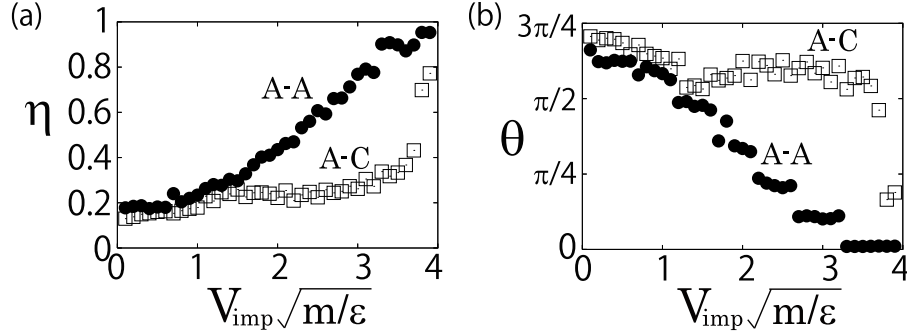


Figure 2.11: (a) Plots of the cluster adsorption parameter η and (b) plots of the contact angle θ as functions of the incident speed for both A-C case (open square) and A-A case (filled circle).

To investigate the effect of the interaction energy on the outcome of impact, we also perform the molecular dynamics simulation in which the LJ parameters of A and C are used for the atoms in the cluster and the atoms of the substrate, respectively. Henceforth, we call this situation A-C case. The Lorentz-Berthelot rule (Eq. (2.2)) is adopted to calculate the cross LJ parameters ϵ_{AC} and σ_{AC} . Other simulation settings are the same as those described in §2.2.

Figure 2.11 shows the cluster adsorption parameter η and contact angle θ as functions of the incident speed for the LJ cluster of 300 atoms. We also plot the data in the case of the LJ parameters of the A-A case. We observe that the cluster adsorption parameter η remains low even if the impact speed is high (Fig. 2.11(a)). We also stress that any A cluster does not become a monolayer film in which θ becomes zero during the deposition onto a C surface. This is because the wetted state of the argon cluster is unfavorable on the crystalline carbon surface, which results from $\epsilon_{AC} < \epsilon$. Thus, it is clear that not only the incident velocity, but also the choice of composites is important to determine the final configuration of the deposited cluster.

2.3.6 Temperature dependence of a deposited Lennard-Jones nanocluster

Critical temperature

The cluster moves toward the substrate by the incident speed $V_{\text{imp}} = 2.0 \sqrt{\epsilon/m}$ and collides with the surface. After the impact, the cluster is deformed and adsorbed on the surface, and the temperature of the deposited cluster is relaxed to the surface temperature. We observe the system for 4000τ after the temperature of the deposited cluster is relaxed.

To investigate the stabilities of the deposited clusters, we introduce the evaporation rate which is defined by

$$\frac{1}{\tau_{\text{ev}}} = \frac{\rho_s}{\tau_v}, \quad (2.16)$$

where ρ_s is the adatom area fraction and $1/\tau_v$ is a probability per unit time for adatom to evaporate from the surface [146]. Because the cluster is deposited on the surface in vacuum, the evaporation rate $1/\tau_{\text{ev}}$ equals zero if the deposited cluster is stable. From the results of our simulation, the evaporation

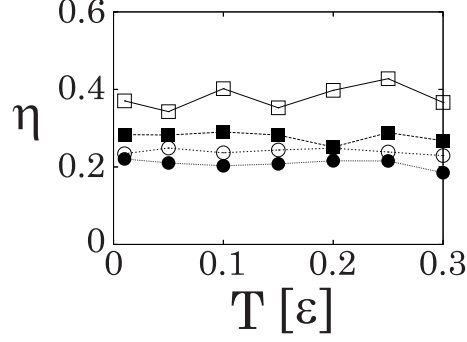


Figure 2.12: Plots of the adsorption parameter η of the deposited cluster as the functions of the temperature for $N = 108$ (open squares), 255 (filled squares), 500 (open circles) and 862 (filled circles), respectively.

rate $1/\tau_{ev}$ equals zero if the temperature is below 0.3ϵ . By contrast, $1/\tau_{ev}$ is finite and the system is not in a steady state if the temperature is larger than 0.3ϵ . Therefore, the deposited cluster is stable only below the critical temperature $T_C \equiv 0.3\epsilon$.

Adsorption parameter and morphology of the deposited cluster

Figure 2.12 displays the temperature dependence of the adsorption parameter η of the deposited cluster. Each value in Fig. 2.12 is averaged over the last 2000τ time steps. The adsorption parameter η is almost independent of the temperature and satisfies $\eta < 1$ for $T < T_C$. It can also be seen that η decreases as the cluster size increases.

Morphology of the deposited cluster

Figure 2.13 exhibits the snapshots of the deposited clusters in the steady state, and Fig. 2.14 displays the temperature dependence of the scaled value R^3/N . Each value in Fig. 2.14 is averaged over the last 2000τ time steps. It can be seen that the contact radius R is almost constant for each cluster size, and it seems that the morphology of the cluster does not depend on the temperature if $T < T_C$.

Structural properties of the deposited cluster

To investigate the structural properties of the deposited cluster, we measure the binding energy and the orientational bond order parameter. The binding energy E_b is defined by the potential energy per atom in the cluster. The orientational bond order parameter is defined by a connecting pair of neighboring atoms in the cluster. This parameter is related to the spherical harmonics function

$$Q_{lm} \equiv Y_{lm}(\theta(r), \phi(r)), \quad (2.17)$$

where $\theta(r)$ and $\phi(r)$ are the polar and azimuthal angles of the bond r with respect to a fixed reference frame. We also average Q_{lm} over all bonds in the cluster as

$$\bar{Q}_{lm} = \frac{1}{N_b} \sum_r Q_{lm}(r), \quad (2.18)$$

where N_b is the total number of bonds. Finally, to make this parameter invariant with respect to rotations of the reference frame, we introduce the second-order invariants as the orientational bond order parameter

$$Q_l \equiv \sqrt{\frac{4\pi}{2l+1} \sum_{m=-l}^l |\bar{Q}_{lm}|^2}. \quad (2.19)$$

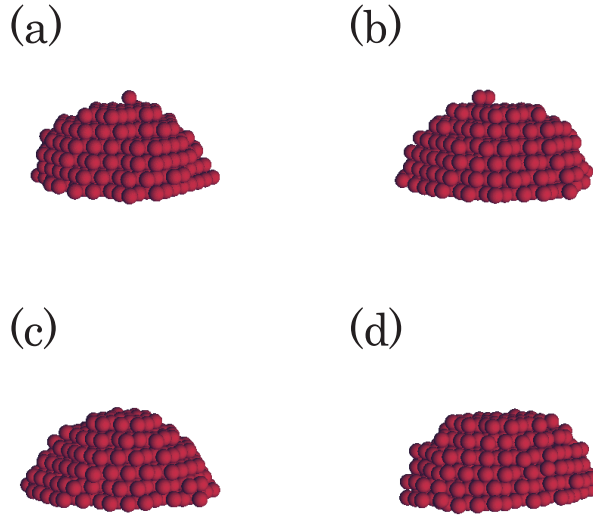


Figure 2.13: (Color online) Snapshots of the deposited cluster at equilibrium. The number of atoms in the cluster is 500. The temperature of the cluster equals (a) 0.01ϵ , (b) 0.1ϵ , (c) 0.2ϵ and (d) 0.3ϵ , respectively.

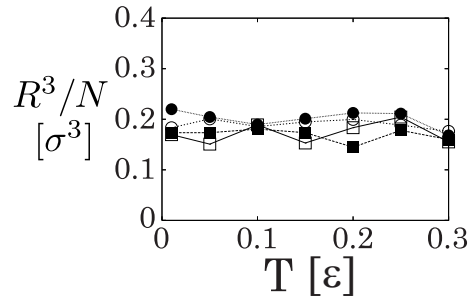


Figure 2.14: Plots of the scaled contact radius R^3/N as the function of the temperature for $N = 108$ (open squares), 255 (filled squares), 500 (open circles) and 862 (filled circles), respectively.

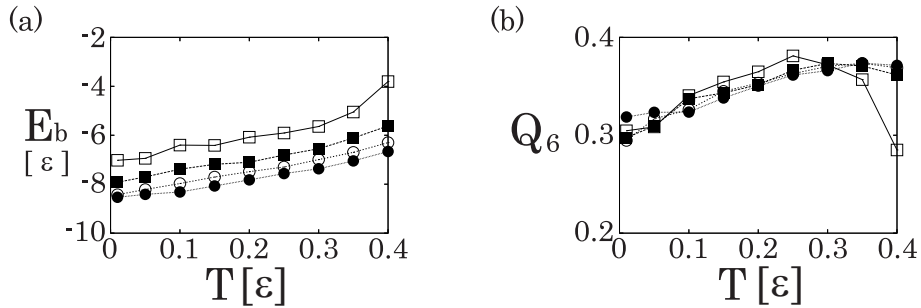


Figure 2.15: Plots of (a) the binding energy E_b and (b) the orientational bond order parameter Q_6 of the deposited cluster as the functions of the temperature for $N = 108$ (open squares), 255 (filled squares), 500 (open circles) and 862 (filled circles), respectively.

It is known that Q_l characterizes the dominant structure in the cluster [147–149].

Figures 2.15 (a) and (b) display the temperature dependence of E_b and Q_6 , respectively. In our simulation, we find that E_b and Q_6 are steady even if the temperature $T > T_C$. Each value in Fig. 2.15 is averaged over the last 2000τ time steps. It can be seen that E_b and Q_6 increases as the temperature increases below T_C . When the temperature becomes larger than T_C , Q_6 decreases as the temperature increases because of the evaporation.

2.4 Discussion and conclusions

In this paper, the incident kinetic energy per atom in the cluster is less than 2 eV. In this case, the damage of the substrate due to the impact of a cluster can be ignored and we considered a single-layer substrate. However, the effect of the interaction between the deposited cluster and the bulk of the substrate is important. In general, the adsorption state is strongly affected by the surface temperature, [150] but the substrate was assumed to be at $T = 0$ before the cluster impact in our simulation. Therefore, the affect of the surface temperature is also important for future study. Moreover, we performed simulation only for one deposition event of the cluster at each incident speed. Thus, we should take an ensemble average of impact processes for future study.

In conclusion, we found that deposited LJ clusters consisting 32, 108, 255, 300, 500, and 862 atoms exhibit a transition from multilayered adsorption to monolayered adsorption at the critical incident speed, $V_{\text{imp}} = 3.3 \sqrt{\epsilon/m}$. From our simulation, we clarified that the deposited clusters are perfectly wetting on the substrate above the critical incident speed. Employing the energy conservation law, we estimated the critical value of the incident speed at which the evaporation begins to occur during the impact. The estimated critical value, $V_{\text{imp}} = 1.7 \sqrt{\epsilon/m}$, exhibits good agreement with our simulation results of ξ . Using the energy conservation law, we also found that the scaled cluster adsorption parameter is independent of the cluster size and is proportional to V_{imp}^2 . These results exhibit good agreement with our simulation results. We performed the Fourier analysis of $g(\psi)$ and found that some modes become unstable for $3.0 \sqrt{\epsilon/m} < V_{\text{imp}} < 4.0 \sqrt{\epsilon/m}$. We also performed the molecular dynamics simulation of the A-C case and we found that the A cluster does not become a monolayer film on the C surface. Thus, we concluded that not only the incident speed, but also the strength of the interaction between the cluster and the substrate is important to form a monolayer film on a substrate. The deposited cluster is stable if $T < T_C$, but the evaporation occurs if $T > T_C$. The morphology of deposited cluster is almost independent of the temperature for $T < T_C$. The binding energy of the deposited cluster E_b increases as the temperature increases. The orientational bond order parameter Q_6 increases as the temperature increases for $T < T_C$, but decreases for $T > T_C$ because of the evaporation.

Chapter 3

Depositions of an argon nanocluster on a free-standing graphene sheet

3.1 Introduction

Graphene is a two-dimensional (2D) atomic layer of carbon atoms on a honeycomb lattice. Recent remarkable experimental techniques have made it possible to observe the motion of a free-standing or suspended graphene sheet [98, 100]. Because electrons in a graphene can travel sub-micrometer distances without scattering, the study of graphene is active to make nanoscale electronic devices [101]. Graphene can be wrapped up into fullerenes and rolled into carbon nanotubes, and thus it is the most fundamental structure of nano-carbon materials [97]. Such flexibility of graphene encourages many researchers to investigate its mechanical properties. A recent experiment has detected the mechanical vibrations of suspended graphene sheets activated by radio frequency voltages, and has observed vibration eigenmodes which are not predicted by the elastic beam theory [99]. In contrast to the electrical activations of graphene, it is also possible to activate the motion of graphene by nanocluster impact [151]. The nanocluster impact can generate high pressure in localized areas of graphene, and it is an appropriate method to verify the elastic theory for the plate deflected by the concentrated force. In addition, nanocluster impact is also important for manufacturing nanoscale electronic devices on a substrate [50, 55, 69, 130, 142]. Therefore, it is necessary *to understand the motion of the graphene induced by a collision with nanocluster* in order to verify the elastic theory and to aim to construct the nanoscale electronic devices on a graphene sheet. However, there are a few studies which investigate the time evolution of the local deformation of the graphene deflected by the nanocluster impact. In this paper, we perform the molecular dynamics (MD) simulation to investigate the time evolution of the deformation of a free-standing graphene sheet deflected by a collision with an argon nanocluster. We find that analytic solutions of the elastic plate well reproduce the results of our MD simulation. We also analyze the time evolution of the temperature profile of the graphene sheet.

The organization of this paper is as follows. In Section 3.2, we introduce our numerical model of the nanocluster impact on a graphene sheet. Section 3.3 consists of three subsections. In Section 3.3.1, we show the time evolution of the deflection of the graphene. In Section 3.3.2, we analyze the time evolution of the deflection. In Section 3.3.3, we analyze the heat-up of the graphene after the impact. We discuss our results in Section 3.4 and conclude in Section 3.5.

3.2 Molecular dynamics simulation of the impact

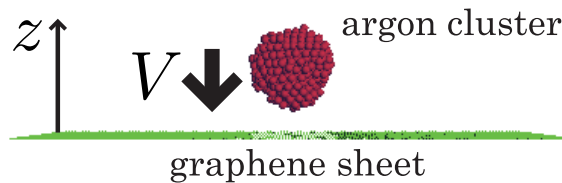


Figure 3.1: (Color online) A snapshot of impact of an argon cluster on a free-standing graphene sheet. The incident cluster contains 500 argon atoms. The graphene sheet contains 16032 carbon atoms on a honeycomb lattice.

To study the dynamical motion of the graphene induced by a collision with an argon cluster, we perform the MD simulation. We adopt the Lennard-Jones (LJ) potential $\phi(u) = 4\epsilon \left[(\sigma/u)^{12} - (\sigma/u)^6 \right]$ for the interaction between two argon atoms with the distance u between two argon atoms, where we use the LJ parameters [152] $\epsilon = 1.03 \times 10^{-2}$ (eV) and $\sigma = 0.340$ (nm). We also adopt LJ potential for the interaction between an argon atom and a carbon atom, where we use the cross parameters of LJ potential ϵ_{int} and σ_{int} , which are defined by the Lorentz-Berthelot rule as $\epsilon_{\text{int}} = \sqrt{\epsilon\epsilon'}$ and $\sigma_{\text{int}} = (\sigma + \sigma')/2$, respectively. Here, $\epsilon' = 2.40 \times 10^{-3}$ (eV) and $\sigma' = 0.335$ (nm) are the LJ

parameters for carbon [153, 154]. Finally, we adopt the Brenner potential, which is widely used for simulations of a graphene and a carbon nanotube, for the interaction between two carbon atoms [126].

Figure 3.1 displays a snapshot of our impact simulation. The graphene involves 16032 carbon atoms on a honeycomb lattice. The bond length of the graphene is 0.142nm and the length of one edge is approximately equal to 20nm. The carbon atoms on the edges parallel to the x -axis are arranged in armchair geometries, and the carbon atoms on the edges parallel to the y -axis are arranged in zigzag geometries [155, 156]. The boundary conditions of the four edges of the graphene are free, and the initial temperature of the graphene is 1.2K. The cluster containing 500 argon atoms is made from argon gas by the temperature quench method [133, 157]. At first, we prepare 500 argon atoms in a periodic box and equilibrate at 119.6K with the number density 1.27nm^{-3} in the gas state. We quench the temperature to 59.8K. After an equilibration, a liquid-like argon cluster is formed. We further quench the temperature to 1.2K to make it rigid, and an amorphous argon cluster is formed [130]. The center of mass of the amorphous argon cluster is placed at 5.1nm above the center of mass of the graphene. The argon cluster is translated with the incident velocity V to collide with the graphene. The incident angle of the argon cluster to the graphene normal is zero.

3.3 Results

3.3.1 Time evolution of the deflection

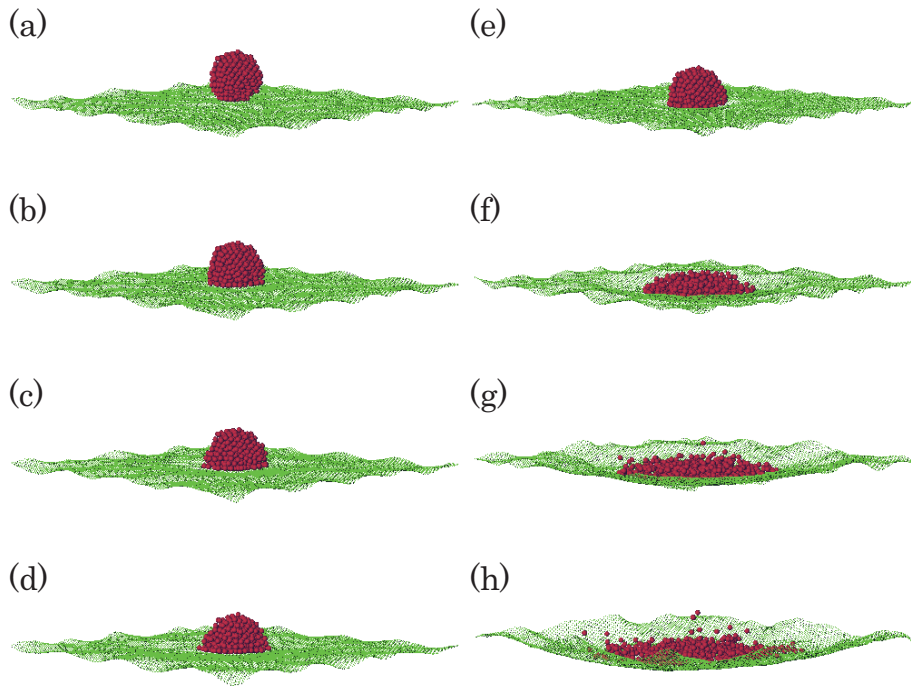


Figure 3.2: The time evolutions of the graphene sheet and argon nanocluster for the incident speed $V = 316$ (m/s) (a)-(d), and $V = 790$ (m/s) (e)-(h), respectively.

Figures 3.2 (a)-(d) and (e)-(h) exhibit the time evolutions of the graphene sheet and argon nanocluster for $V = 316$ (m/s) and $V = 790$ (m/s), respectively. Let us demonstrate the motion of the graphene induced by the collision with the argon cluster in the case of $V = 316$ (m/s). Figures 3.3 display the time evolution of the deflection of the graphene ζ as a function of x and y coordinates. In

this figures, we divide the xy plane into 32×32 cells and average over z -components of the positions of carbon atoms in the center-of-mass frame. We define $t = 0$ as the time at which the argon cluster contacts the graphene sheet. At the impact, the circular region around the center of the graphene is bended by the incident argon cluster (Figs. 3.3 (a)), and the transverse deflection wave is isotropically propagated in the graphene (Figs. 3.3 (b)). In the laboratory system, the graphene is moved downward and immediately reaches the uniform motion along the z -axis with the speed 28.4m/s. During the impact, the incident argon cluster adsorbs on the graphene and does not rebound. Figures 3.4 display the time evolution of ζ for the incident speed $V = 790$ (m/s). At the impact, the circular region around the center of the graphene is strongly bended by the incident argon cluster (Figs. 3.4 (a)), and the transverse deflection wave is observed (Figs. 3.4 (b)). During the impact, the incident argon cluster bursts into fragments and some fragments are scattered and the rest of fragments adsorb on the graphene. We have also examined the cases of $V = 158, 474,$ and 632 (m/s), and the bending formation and the propagation of transverse deflection wave are also observed. In all cases, the deflection wave in the graphene passes through the boundary without reflection, and the graphene ripples after the impact. We have never observed any defect formations in the graphene sheet.

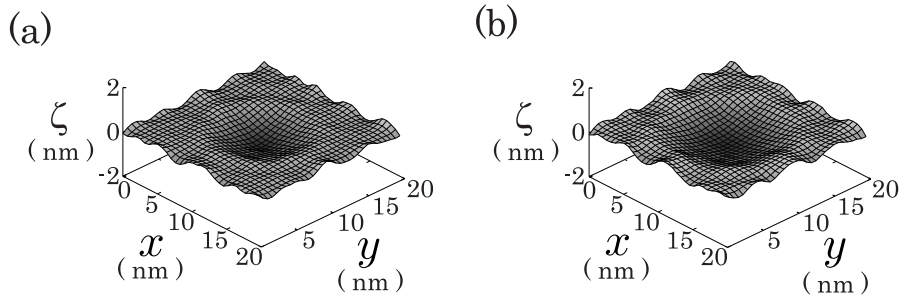


Figure 3.3: The deflection of the graphene sheet ζ at (a) 2.2 ps and (b) 2.8 ps after the initial hitting. The incident cluster contains 500 argon atoms, and the incident speed is 316m/s.

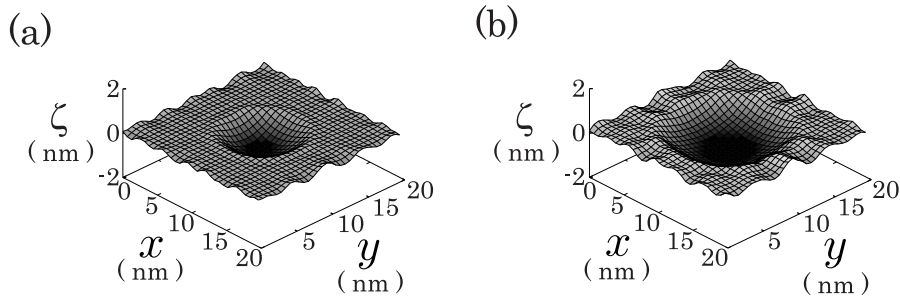


Figure 3.4: The deflection of the graphene sheet ζ at (a) 2.2 ps and (b) 2.8 ps. The incident cluster contains 500 argon atoms, and the incident speed is 790m/s.

3.3.2 Analysis of the deflection

Equation of motion

To analyze the result of our simulation, we examine the linear theory of the elasticity in description of the deflection of the graphene [158, 159]. Because the elastic properties of a 2D hexagonal structure are isotropic [158], we ignore the anisotropic properties of the graphene sheet. Thus, the equation of motion for the deflection is given by

$$\rho \ddot{\zeta}(r, t) + \frac{h^3 E}{12(1 - \mu^2)} \Delta^2 \zeta(r, t) = p(r, t), \quad (3.1)$$

Here, $\rho = 7.59 \times 10^{-7}$ (kg/m²) is the mass per unit area of the graphene, and $\zeta(r, t)$ represents $\partial^2 \zeta(r, t) / \partial t^2$. Because graphene is a single atomic layer of carbon, its thickness h is sometimes set to be the diameter of a carbon atom, 0.335 nm. However, Yakobson *et al.* indicated that $h = 0.066$ (nm) should be used in their simulation of single-walled carbon nanotubes [108]. We still do not have any consensus on the proper value of h [102–105, 110]. Thus, to avoid ambiguous definition of the thickness, we use the thickness and the elastic moduli which are directly obtained from the analysis of the Brenner potential. Following Ref. 26, we use the thickness, Young's modulus, and Poisson's ratio as $h = 0.0874$ (nm), $E = 2.69$ (TPa), and $\mu = 0.412$, respectively. The right hand side of Eq. (3.1) is the external pressure due to the argon cluster impact. Because the deflection is symmetric with respect to the z -axis, we assume that ζ and p depend on time t and the distance from the z -axis r .

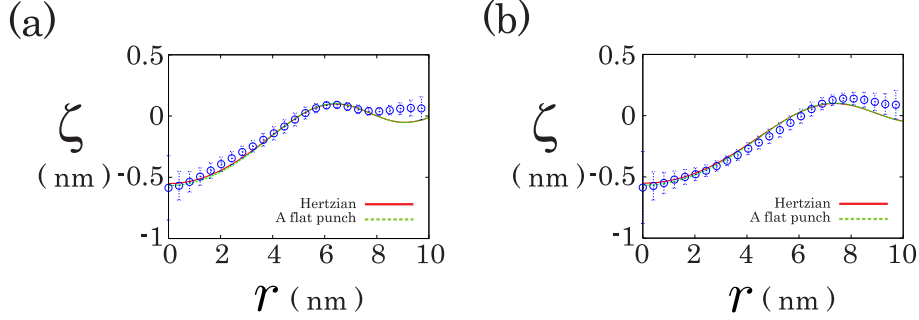


Figure 3.5: (Color online) The MD simulation results of the mean deflection of the graphene (open circle) which are averaged over the azimuthal coordinate, and the solutions of the equation of motion, i.e. Eqs. (3.6) (red solid line) and (3.9) (green broken line) at (a) 2.2 ps and (b) 2.8 ps. The incident cluster contains 500 argon atoms, and the incident speed is 316 m/s. The magnitude of the impulse is 1.96×10^{-10} N · ps.

Hertzian contact pressure

Although the external pressure changes during the impact, we simply assume that $p(r, t)$ is an impulsive pressure with the distribution of the Hertzian contact stress. Thus, we may assume

$$p(r, t) = -\frac{3F}{2\pi a^2} \sqrt{1 - \left(\frac{r}{a}\right)^2} \Theta(a - r) \delta(t), \quad (3.2)$$

where F and a are the impulse and the contact radius of the incident argon cluster [158]

$$a = \left[\frac{3FR}{4} \left\{ \frac{1 - \mu^2}{E} + \frac{1 - \mu'^2}{E'} \right\} \right]^{1/3}, \quad (3.3)$$

respectively. Here, $\delta(t)$ is Dirac's delta function, and $\Theta(a - r)$ is the Heaviside function which is defined as $\Theta(a - r) = 1$ for $r < a$ and $\Theta(a - r) = 0$ for $r > a$. The mean radius, Young's modulus, and Poisson's ratio of the argon cluster are $R = 1.6$ (nm), $E' = 3.69$ (GPa), and $\mu' = 0.396$, respectively, which are estimated from our another MD simulation [160, 161]. In addition, we assume that the contact area of radius a moves downward with the speed V at the impact. Thus, the initial conditions of the deflection are $\zeta(r, 0) = 0$ and $\dot{\zeta}(r, 0) = -V\Theta(a - r)$. Because we consider the behaviors in the vicinity of the center of the graphene, we solve Eq. (3.1) as if the graphene sheet is infinitely large. The Fourier transform and the Laplace transform of Eq. (3.1) yield

$$\hat{\zeta}_k(s) = -\frac{H(k)}{s^2 + Dk^4}, \quad (3.4)$$

where $D \equiv h^3 E / 12\rho(1 - \mu^2)$. Here, we introduce the function

$$H(k) \equiv \frac{3F \sin(ak) - ak \cos(ak)}{\rho (ak)^3} + 2\pi a V \frac{J_1(ak)}{k}, \quad (3.5)$$

where $J_n(x)$ is the Bessel function for an integer n . Here, we represent the Laplace transform and the Fourier transform as $\hat{\zeta}_k(s) \equiv \int_0^\infty \zeta_k(t) e^{-st} dt$ and $\zeta_k(t) \equiv \int_{-\infty}^\infty d\mathbf{k} \zeta(r, t) e^{-i\mathbf{k}\cdot\mathbf{x}}$, respectively. The inverse Laplace transform and the inverse Fourier transform of Eq. (3.4) yield

$$\zeta(r, t) = - \int_0^\infty H(k) J_0(kr) \frac{\sin(\sqrt{D}k^2 t)}{\sqrt{D}k} dk. \quad (3.6)$$

A flat punch pressure

If we adopt a flat punch impulsive pressure

$$p(r, t) = -\frac{F}{\pi a^2} \Theta(a - r) \delta(t) \quad (3.7)$$

instead of Eq. (3.2), the Fourier transform and the Laplace transform of Eq. (3.1) yield

$$\hat{\zeta}_k(s) = -\frac{2H_0 J_1(ak)}{ak} \frac{1}{s^2 + Dk^4}, \quad (3.8)$$

where we introduce the constant $H_0 \equiv \rho^{-1} F + \pi a^2 V$. In this case, the solution of Eq. (3.8) is

$$\zeta(r, t) = -\frac{2H_0}{a} \int_0^\infty J_0(kr) J_1(ak) \frac{\sin(\sqrt{D}k^2 t)}{\sqrt{D}k^2} dk. \quad (3.9)$$

Figures 3.5 display the time evolution of the deflection $\zeta(r, t)$ in the case of $V = 316$ (m/s). In this figures, the open circles are our MD simulation results which are averaged over the azimuthal coordinate. The red solid and green broken lines represent Eqs. (3.6) and (3.9), respectively. Here, we use $F = 1.96 \times 10^{-10}$ (N · ps) for both Eq. (3.6) and Eq. (3.9). We have also examined the deflection of the graphene in the case of $V = 158$ (m/s), and we find that the time evolution of $\zeta(r, t)$ is well described by Eqs. (3.6) and (3.9) with $F = 1.25 \times 10^{-10}$ (N · ps). However, in the cases of $V = 474, 632$ and 790 (m/s), Eqs. (3.6) and (3.9) are no longer applicable because the incident argon cluster bursts into many fragments which collide with the graphene, and the distribution of the external pressure can neither be approximated by the Hertzian contact stress nor a flat punch pressure.

3.3.3 Analysis of the heat-up

To study heat up of the graphene, we introduce the local temperature. We divide the graphene into 64×64 cells along the x - and y -axes and define the temperature of the j -th cell as

$$T_j = \frac{m}{3k_B N_j} \sum_{i=1}^{N_j} (\mathbf{v}_i - \mathbf{u}_j)^2, \quad (3.10)$$

where k_B and $m = 1.99 \times 10^{-26}$ (kg) are the Boltzmann constant and the mass of carbon atom, respectively. In Eq. (3.10), N_j , \mathbf{v}_i and \mathbf{u}_j are the number of carbon atoms in the j -th cell, the velocity of the i -th carbon atom which is in the j -th cell and the mean velocity of the j -th cell, respectively. The mean velocity of the j -th cell is defined as

$$\mathbf{u}_j = \frac{1}{N_j} \sum_{i=1}^{N_j} \mathbf{v}_i. \quad (3.11)$$

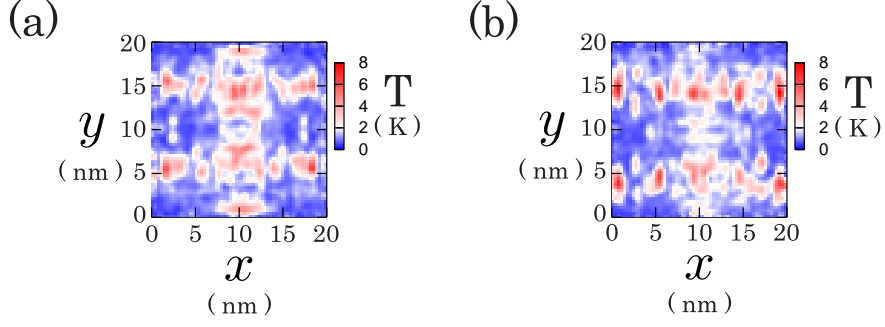


Figure 3.6: The temperature profile of the graphene sheet $T(x, y)$ at (a) 2.2 ps and (b) 2.8 ps after the initial hitting. The incident cluster contains 500 argon atoms, and the incident speed is 316m/s.

In order to take a sample average of T_j , we rotate the nanocluster around the line before the impact, where we use the different angle for each sample. Here, the line is parallel to the z -axis and intersects at the center of mass of the nanocluster. If we project the 64×64 cells to the xy plane, Eq. (3.10) approximately represents the temperature profile $T(x, y)$. Figures. 3.6 display the time evolution of $T(x, y)$ which is averaged over 20 samples in the case of $V = 316$ (m/s). Although the thermal conductivity of a 2D hexagonal structure is isotropic [162], the results of $T(x, y)$ are anisotropic.

Let us explain the anisotropic profile of $T(x, y)$. The nanocluster collides with the graphene in the vicinity of the center of mass of the graphene (X, Y) . By the impact, the vicinity of (X, Y) is heated up and the heat current \mathbf{q} flows from (X, Y) to the edge of the graphene. Then, \mathbf{q} is symmetrical with respect to (X, Y) , and we adopt (X, Y) for the origin. In such an irreversible process, thanks to the least dissipation principle, the rate of the entropy production

$$\mathcal{D} = - \int_A \kappa^{-1} \mathbf{q}^2 dA \quad (3.12)$$

is expected to be minimum, where A and κ are the area of the graphene and the heat conductivity per unit area of the graphene, respectively [163]. If we assume that κ is a constant, the variation $\delta\mathcal{D} = 0$ leads $\nabla \cdot \mathbf{q} = 0$ [163]. Therefore, from Fourier's law of heat conduction, the deviation of the temperature $\delta T = T(x, y) - T_0$ satisfies Laplace's equation $\Delta\delta T = 0$. Here, T_0 is the temperature of the graphene before the impact. Because δT is finite at (X, Y) , the general solution of Laplace's equation is

$$\delta T(r, \theta) = const. + \sum_{n=1}^{\infty} r^n a_n \cos(n\theta + \phi) \quad (3.13)$$

in the polar coordinate, where a_n and ϕ are the integral constants [164]. Because \mathbf{q} is symmetrical with respect to (X, Y) , the integer n satisfies $\cos(n(\theta + \pi) + \phi) = \cos(n\theta + \phi)$ and $\sin(n(\theta + \pi) + \phi) = \sin(n\theta + \phi)$. Thus, n should be even. Therefore, $\delta T(r, \theta)$ is distributed around (X, Y) as

$$\delta T(r, \theta) = const. + \sum_{m=1}^{\infty} r^{2m} a_{2m} \cos(2m\theta + \phi). \quad (3.14)$$

In Fig. 3.6 (a), the heated region can be seen as a quadrupole distribution around (X, Y) which is the case of $m = 1$ in Eq. (3.14). On the other hand, in Fig. 3.6 (b), the heated region is no longer distributed as Eq. (3.14). In this case, it seems that the least dissipation principle is no longer correct, and it is necessary to solve the heat equation with the boundary conditions correctly.

3.4 Discussion

Although Eqs. (3.6) and (3.9) seem to well describe the results of our MD simulation, the solution does not satisfy the boundary conditions, and these are not applicable except for the case that deformations are localized in the vicinity of the center of the graphene sheet, i.e. immediately after the impact. Note that it is difficult to obtain an analytic solution of Eq. (3.1) which satisfies the completely free boundary conditions [165, 166]. If we simply estimate the magnitude of the impulse from the change in momentum of the incident argon cluster, $F = 3.59 \times 10^{-10}$ (N · ps) which is about two times larger than the fitted value in Figs. 3.5. However, the value is over-estimated, because the loading force can change during the impact and the dissipative force plays important role for the collision of clusters [87, 93]. In the case of $V \geq 400$ (m/s), the impact processes are further complicated by many fragments of the argon cluster, and Eqs. (3.6) and (3.9) are no longer correct. Therefore, it is necessary to improve the functional form of $p(r, t)$. Note that if we use $h = 0.335$ (nm) in Eqs. (3.6) and (3.9), the wave propagates much faster than the actual propagation observed in our MD simulation. Thus, the thinner thickness $h = 0.0874$ (nm) is more appropriate. The analysis based on the least dissipation principle reproduces our simulation result of the temperature profile in the early stage of impact. However, in order to describe the time evolution of the temperature profile, it is necessary to solve the heat equation with appropriate boundary conditions.

3.5 Conclusion

In conclusion, we perform the molecular dynamics simulation of the graphene sheet induced by a collision with an argon nanocluster, and the bending formation and the propagation of transverse deflection wave are observed. We find that the linear theory of the elasticity well explains the time evolution of the deflection of the graphene, where the deflection is represented by using the analytic expressions Eqs. (3.6) and (3.9). In addition, we conclude from the analysis of the motion of the graphene that the actual thickness is much thinner than the diameter of a carbon atom. We also analyze the time evolution of the temperature profile, and find that the analysis based on the least dissipation principle reproduces our simulation result in the early stage of impact. We believe that the predictions of the bending formation and propagation of transverse deflection wave are necessary for the construction of the nanoscale electronic devices on a graphene sheet.

Chapter 4

Negative normal restitution coefficient for nanocluster collisions

4.1 Introduction

Inelastic collisions, where a part of mechanical energy of colliding bodies transforms into heat, are common in nature and industry. Avalanches, rapid granular flows of sand, powders or cereals may be mentioned as pertinent examples [82, 83]. Moreover, inelastic collisions define basic properties of astrophysical objects, like planetary rings, dust clouds, etc. An important characteristic of such collisions is the so-called normal restitution coefficient e . According to a standard definition, it is equal to the ratio of the normal component of the rebound speed, \mathbf{g}' (prime states for the post-collision value), and the impact speed, \mathbf{g}

$$e = -\frac{\mathbf{g}' \cdot \mathbf{n}}{\mathbf{g} \cdot \mathbf{n}}. \quad (4.1)$$

The unit inter-center vector $\mathbf{n} = \mathbf{r}_{12}/|\mathbf{r}_{12}|$ at the *collision instant* ($\mathbf{r}_{12} = \mathbf{r}_1 - \mathbf{r}_2$) specifies the impact geometry. Since particles bounce in the direction, opposite to that of the impact, e is positive, $e > 0$, and since the energy is lost in collisions, e is smaller than one, that is, $0 \leq e \leq 1$. This is a common statement in the majority of mechanical textbook, where it is also claimed that e is a material constant. Recent experimental and theoretical studies show, however, that the concept of a restitution coefficient is more complicated: First, it depends on an impact speed [84–87], second, it can exceed unity for a special case of oblique collisions with elastoplastic plate [88–90], where the energy of normal motion can increase at the expense of the energy of tangential motion [88–90]. Still, it is believed that $e \leq 1$ for a true head-on collision.

The concept of a restitution coefficient, as a basic one of the classical mechanics, has been introduced long ago by Newton; it addresses an impact of macroscopic bodies. The increasing interest to nanoparticles, inspired by its industrial significance, raises an important question, to what extent the macroscopic concepts are applicable and whether they acquire new features at a nanoscale. The collisions of nanoclusters has been studied in detail numerically [72, 91–95]. It was observed that the surface effects, due to the direct inter-cluster van der Waals interactions, play a crucial role: The majority of collisions of homogeneous clusters, built of the same atoms, lead to a fusion of particles [91, 92]; they do not fuse for high impact speeds, but disintegrate into pieces [91, 92]. This complicates the analysis of restitutive collisions, which may be more easily performed for particles with a reduced adhesion. Among possible examples of such particles are clusters of covalently bonded atoms, especially when their surface is coated by atom of different sort, as for H-passivated Si nanospheres [72]. These particles can rebound from a substrate, keeping their form after an impact unaltered [72]. The bouncing nanoclusters demonstrate a surprising effect – the normal restitution coefficient can exceed unity even for strictly head-on collisions [93].

In this Letter we investigate the oblique impact of nanoclusters with the reduces adhesion by means of Molecular Dynamics (MD) and theoretically, using concepts of continuum mechanics. Unexpectedly, we have found that the normal restitution coefficient, as defined by Eq. (4.1), acquires for large incident angles negative values, $e < 0$. We explain this effect by the reorientation of the contact plane during an impact and quantify it. Moreover, we propose a modified definition of e , which preserves its initial physical meaning and yields always positive values. To describe the collision of nanoclusters we develop a continuum theory. Surprisingly, the macroscopic approach quantitatively agrees with MD even at nanoscale.

4.2 MD simulations

We study two models - a simplified model (A), which mimics interactions of nanoclusters with the reduced adhesion and realistic model (B) for interaction of nanoclusters with covalently bonded atoms – H-passivated Si nanospheres. For the model A, which is less computationally expensive, we adopt the Lennard-Jones (LJ) potential $\phi(r) = 4\epsilon \left[(\sigma_{LJ}/r)^{12} - (\sigma_{LJ}/r)^6 \right]$ for the interaction between two

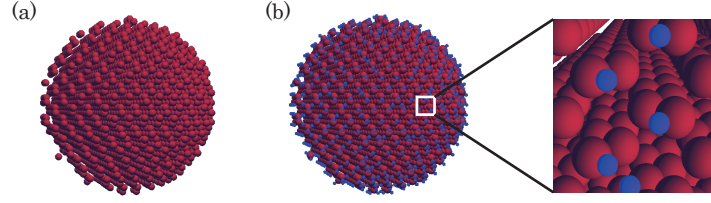


Figure 4.1: Si nanocluster (a) before hydrogen passivated and (b) after hydrogen passivated and its surface. Red and blue particles represent Si and H atoms, respectively.

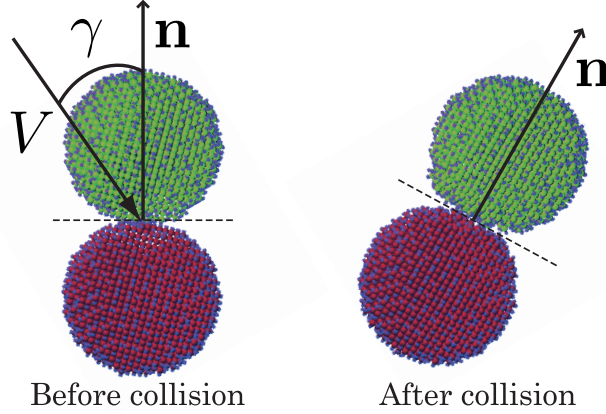


Figure 4.2: (Color online) Initial (left) and final stage (right) of the nanocluster collision. The initial relative velocity is $\mathbf{v}_{12}(0) = \mathbf{V}$ and the incident angle is γ . The unit normal \mathbf{n} specifies the orientation of the contact plane. For large γ a noticeable reorientation of this plane is observed. Here the collision of H-passivated Si nanospheres (model B) is shown.

atoms in the same cluster and the modified LJ potential $\phi_{\text{int}}(r) = 4\epsilon \left[(\sigma_{\text{LJ}}/r)^{12} - c(\sigma_{\text{LJ}}/r)^6 \right]$ for the interaction between atoms in two different clusters. Here the cohesive parameter $c = 0.2$ controls the adhesive force [93–95] between clusters, while ϵ , σ_{LJ} , and r are, respectively, the depth of potential well, the diameter of the repulsive core, and the distance between two atoms. The nanoclusters of $N = 500$ atoms were prepared by the two step temperature quench to obtain a rigid amorphous particle [130]. The radius of nanocluster $d/2$ was defined as the maximum distance between the center of mass of the nanocluster and the atom on the surface, so we find $d = 10.46 \sigma_{\text{LJ}}$. For the model B we adopt the Tersoff potential [120–125] for the covalent Si-Si, Si-H, and H-H bondings. The Si nanospheres, containing 2905 Si atoms arranged in a diamond structure (Fig.4.1 (a)), are fully coated by 852 H atoms (Fig.4.1 (b)). The diameter of Si nanosphere is about $d = 4.8$ nm.

We fix the modulus of the relative inter-cluster velocity $\mathbf{v}_1(0) - \mathbf{v}_2(0) = \mathbf{v}_{12}(0) = \mathbf{V}$ and set it to $V = 1.0 \sqrt{\epsilon/m}$ and 1850 m/s for the model A and B, respectively. We vary the incident angle γ between \mathbf{n} and \mathbf{V} (see Fig. 4.2), so that the normal impact velocity, $V_n = V \cos \gamma$ is changed. The nanoclusters do not rotate before an impact and have zero angular velocities, $\omega_1(0) = \omega_2(0) = 0$. To make an ensemble average, we randomly turn one of the clusters around the axis, passing through its center and perpendicular to the contact plane. Due to rough atomic surfaces of the clusters, this results in varying contact configurations at each impact. Hence, for every incident angle γ we perform averaging over 100 collisions with different contact conditions for model A and over 10 collisions for model B. The clusters' deformation during an impact is quantified by the normal displacement, $\xi_n(t) = d - |\mathbf{r}_{12}(t)| = d - r_{12}(t)$. We define the beginning of a collision at $t = 0$ and the end at $t = t_c$ through the conditions, $\xi_n(0) = \xi_n(t_c) = 0$.

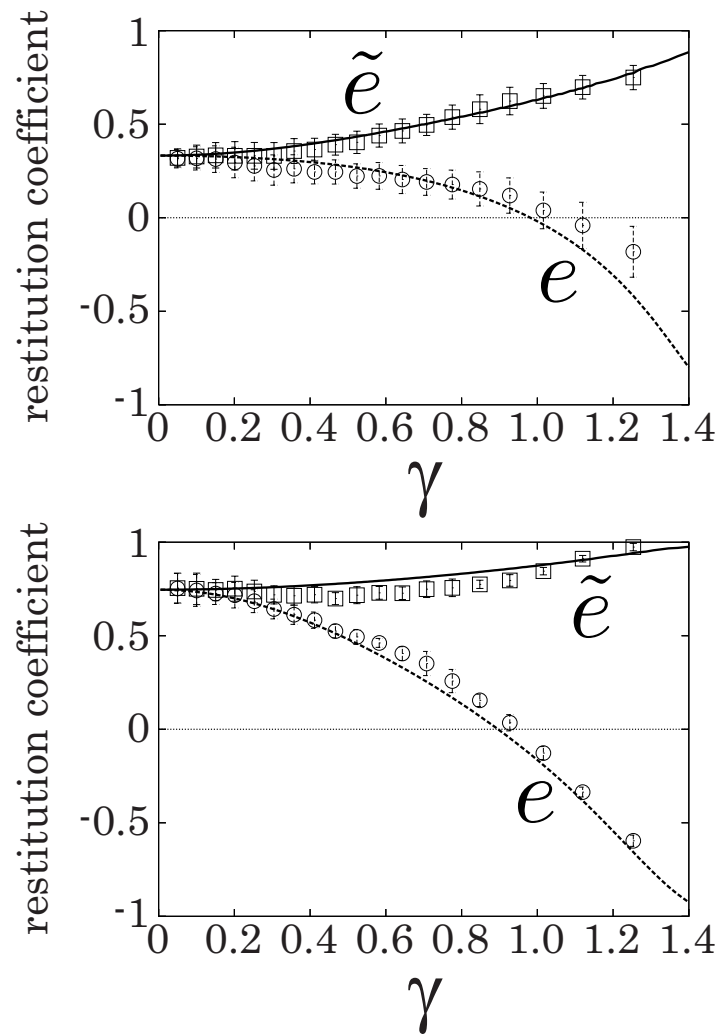


Figure 4.3: Dependence on the incident angle γ of the normal restitution coefficients e , and \tilde{e} according to the standard definitions (4.4) and modified definition (4.5). Open circles and squares are respectively the MD results for e and \tilde{e} , while dashed and solid lines correspond to theoretical predictions. Upper panel refers to the model A and lower panel – to the model B. Note that the coefficient \tilde{e} is always positive.

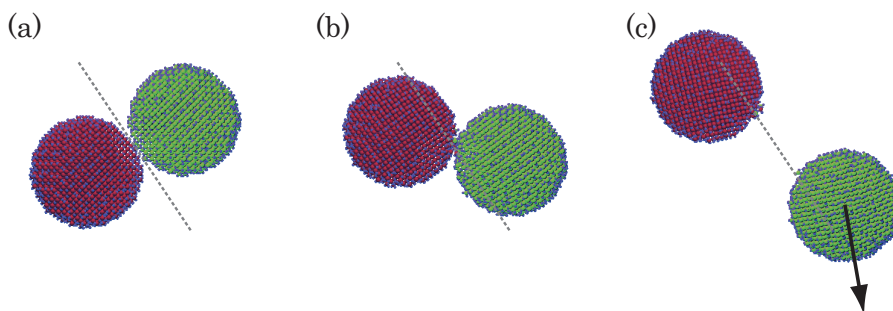


Figure 4.4: Colliding two H-passivated Si nanoclusters, (a) before collision, (b) during collision and (c) after collision, respectively. Gray broken line is the contact line in the xy plane, and the arrow represents the moving direction. The incident angle is $\gamma = 1.1$ and the normal restitution coefficient e is negative.

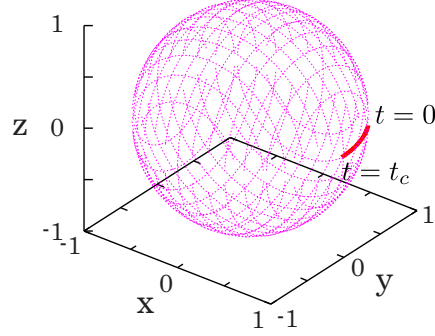


Figure 4.5: The three dimensional plot of the trajectory of $\mathbf{n}(t)$ from $t = 0$ to $t = t_c$.

Simulation results for the normal restitution coefficient for the models A and B are shown in Fig. 4.3 (upper and lower panel respectively). As it is seen from the figure, the restitution coefficient e , defined by Eq. (4.1) becomes negative for large incident angles γ . Figure 4.4 shows the time development of colliding two nanoclusters for the model B with the incident angle $\gamma = 1.1$. Such unusual behavior of e at nanoscales may be understood if we notice that the orientation of the contact plane, characterized by the unit vector $\mathbf{n}(t) = \mathbf{r}_{12}(t)/r_{12}(t)$, significantly alters during the collision, Fig.4.2. (Figure 4.5 is the three dimensional plot of the trajectory of $\mathbf{n}(t)$ from $t = 0$ to $t = t_c$.) This is quantified by the angle α between the initial and final orientations of $\mathbf{n}(t)$,

$$\cos \alpha = \mathbf{n}(0) \cdot \mathbf{n}(t_c). \quad (4.2)$$

The dependence of α on the incident angle γ is shown in Fig. 4.6. If α is large, the normal restitution coefficients becomes negative, Fig. 4.3.

4.3 Modified definition of e

To analyze this effect, consider the relative velocity of particles at their contact,

$$\mathbf{g} = \mathbf{v}_{12} + \frac{d}{2} [\mathbf{n} \times \boldsymbol{\omega}_{12}] = -\dot{\xi}_n \mathbf{n} + r_{12} \dot{\mathbf{n}} + \frac{d}{2} [\mathbf{n} \times \boldsymbol{\omega}_{12}], \quad (4.3)$$

where $\boldsymbol{\omega}_{12} \equiv \boldsymbol{\omega}_1 + \boldsymbol{\omega}_2$ and we use $\mathbf{v}_{12} = \dot{\mathbf{r}}_{12}$ with $\mathbf{r}_{12} = \mathbf{n}(d - \xi_n)$. In the standard definition of e and theoretical studies of an oblique impact [167], \mathbf{n} is taken at the collision instant, that is, its reorientation during the impact is ignored. In experiments, the normal \mathbf{n} is also determined only once, at the beginning of an impact [168, 169], $\mathbf{n} = \mathbf{n}(0)$. Neglecting angular velocities (note that $\boldsymbol{\omega}_{1/2}(0) = 0$) we find for the restitution coefficient:

$$e = -\frac{\mathbf{g}(t_c) \cdot \mathbf{n}(0)}{\mathbf{g}(0) \cdot \mathbf{n}(0)} = \left| \frac{\dot{\xi}_n(t_c)}{\dot{\xi}_n(0)} \right| \cos \alpha - \frac{d \sin \alpha \dot{\alpha}}{V \cos \gamma}, \quad (4.4)$$

where we take into account that $\mathbf{g}(0) \cdot \mathbf{n}(0) = -\dot{\xi}_n(0) = -V \cos \gamma < 0$, that $r_{12}(t_c) = d$ and that $\dot{\xi}_n(t_c) < 0$. For head-on collisions, when $\gamma \rightarrow 0$ and $\alpha \rightarrow 0$ (see Fig. 4.6) the second term in the r.h.s. of Eq. (4.4) is negligible and e is positive. For oblique impacts γ and α are large and the second term prevails, yielding a negative e .

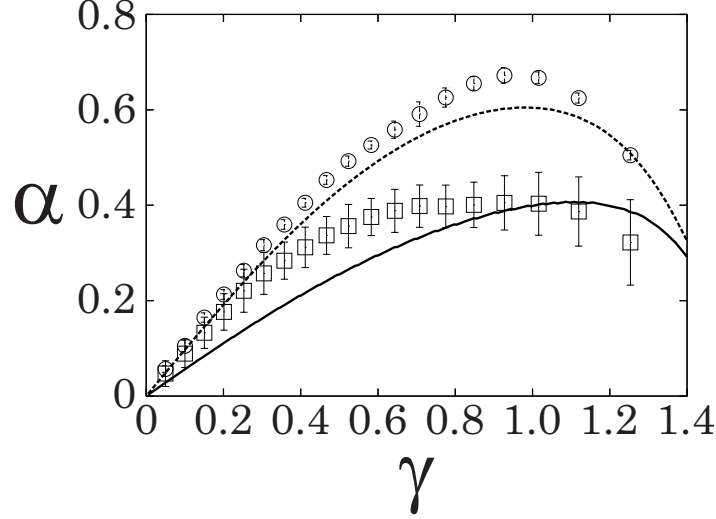


Figure 4.6: Dependence of the angular displacement $\alpha = \arccos[\mathbf{n}(0) \cdot \mathbf{n}(t_c)]$ of the unit normal \mathbf{n} , Eq. (4.2), on the incident angle γ . Open squares and circles are the MD results for the model A and B, respectively. Solid and broken lines are the corresponding theoretical predictions, $\alpha = \int_0^{t_c} \Omega(t) dt$ (see text for detail).

Hence, the negative restitution coefficient is a consequence of a significant reorientation of a contact plane during a collision. For hard particles with a small collision duration the reorientation of \mathbf{n} is small and may be neglected [167]; this usually holds true for macroscopic bodies. In the case of nanoclusters, however, the duration of their impact t_c is relatively large and the reorientation of the contact plane is significant.

As it follows from the Eq. (4.4), the standard definition of e characterizes not only the normal motion along $\mathbf{n}(t)$ (the first term in the r.h.s. of Eq. (4.4)), but also the change of the normal $\mathbf{n}(t)$ (the second term in the r.h.s. of Eq. (4.4)). Therefore, it is worth to define the restitution coefficient, which describes pure normal motion. The respective modification of the standard definition reads:

$$\tilde{e} = -\frac{\mathbf{g}(t_c) \cdot \mathbf{n}(t_c)}{\mathbf{g}(0) \cdot \mathbf{n}(0)} = \left| \frac{\dot{\xi}_n(t_c)}{\dot{\xi}_n(0)} \right|. \quad (4.5)$$

Here we use Eq. (4.3) for $t = t_c$ and take into account that $\dot{\mathbf{n}} \cdot \mathbf{n} = 0$ for a unit vector \mathbf{n} . Note, that the modified restitution coefficient \tilde{e} is always positive, Fig. 4.3. It can be also seen from Fig. 4.3 that the magnitude of \tilde{e} for an oblique impact (for large γ) is significantly larger than that for a head-on collision. In what follows we explain the observed behaviors of e and \tilde{e} using a simple theoretical model, based on continuum mechanics approach.

4.4 Theory of an oblique impact

Consider a non-inertial frame, rotating with the angular velocity $\boldsymbol{\Omega}$, perpendicular \mathbf{n} , so that $\dot{\mathbf{n}} = \boldsymbol{\Omega} \times \mathbf{n}$. To compute the normal force acting between two nanoclusters we apply the impact theory for macroscopic viscoelastic adhesive spheres [86, 87]. It contains the JKR force [81], which accounts for elastic interactions via the Herizian force F_H and for adhesive interactions via the Boussinesq force F_B ,

$$F_H - F_B = \frac{4a^3}{Dd} - \sqrt{\frac{6\pi\sigma}{D}} a^{3/2}. \quad (4.6)$$

It also contains the dissipative force [87],

$$F_D = \dot{a}\eta \left(\frac{12a^2}{Dd} - \frac{3}{2} \sqrt{\frac{6\pi\sigma}{D}} a^{1/2} \right). \quad (4.7)$$

Here, a is the contact radius of the colliding nanoclusters, related to the normal displacement ξ_n as

$$\xi_n = \frac{4a^2}{d} - \sqrt{\frac{8\pi\sigma Da}{3}}, \quad (4.8)$$

and $D = (3/2)(1 - \nu^2)/Y$ is the elastic constant with the Young modulus Y and the Poisson ratio ν . From the independent numerical simulations we estimate $Y = 88.3 \text{ } \epsilon/\sigma_{LJ}^3$ and $\nu = 0.396$ for model A, and $Y = 283 \text{ GPa}$ and $\nu = 0.166$ for model B [161]. The surface tension σ may be expressed via Hamaker constant A_H and the equilibrium distance between atoms at the interface z_0 as $\sigma \simeq A_H/24\pi z_0^2$. We obtain $\sigma = 0.0246 \text{ } \epsilon/\sigma_{LJ}^2$ and 0.046 N/m for the models A and B, respectively. The dissipative constant η , which accounts for the viscoelasticity of the particles' material [86] is used here as a fitting parameter. In the present simulations a good agreement is obtained by choosing $\eta = 0.65 \sigma_{LJ} \sqrt{m/\epsilon}$ and 1.62 fs for models A and B, respectively.

In the non-inertial frame, the inertial force must be also taken into account. Its normal component reads [170],

$$F_I = 2\mu \mathbf{v}_{12} \cdot \dot{\mathbf{n}}(t) - \mu x_{12} |\dot{\mathbf{n}}(t)|^2, \quad (4.9)$$

where $\mu = Nm/2$ is the reduced mass of the nanoclusters. If we again neglect the angular velocities of particles in the collision (since $\omega_{1/2}(0) = 0$), that is, if we assume that the two clusters at a contact move together as a solid dumbbell, we can exploit the conservation of the angular momentum in the form,

$$\mu r_{12}^2 \Omega = \mu V \sin \gamma d, \quad (4.10)$$

where we take into account that $\mathbf{n} \cdot \Omega = 0$. This yields $\Omega(t) = V \sin \gamma d / r_{12}^2(t)$ and the inertial force,

$$F_I = \frac{\mu V^2 d^2}{r_{12}^3} \sin^2 \gamma. \quad (4.11)$$

Combining Eqs. (4.6) – (4.11) we obtain the equation of motion for ξ_n :

$$\mu \frac{d'^2}{dt^2} \xi_n + F_H - F_B + F_D + \frac{\mu V^2 d^2}{(d - \xi_n)^3} \sin^2 \gamma = 0, \quad (4.12)$$

where d'/dt denotes the time derivative in the non-inertial frame. Solving Eq. (4.12) for $\xi_n(t)$, we obtain \tilde{e} as it follows from Eq. (4.5). Taking into account that $\alpha = \Omega(t_c)$ we obtain from Eq. (4.4) the relation between the standard and modified restitution coefficients,

$$e = \tilde{e} \cos \alpha - \tan \gamma \sin \alpha. \quad (4.13)$$

The last equation together with the relation $\alpha = \int_0^{t_c} \Omega(t) dt$ may be used to compute the standard coefficient e . The theoretical predictions for the coefficients e and \tilde{e} are shown on the upper and lower panels of Fig. 4.3 respectively. The agreement between our theory, which has only one fitting parameter, and MD simulations is rather good. We find that the restitution coefficient of H-passivated Si nanospheres is well reproduced by our macroscopic theory for the incident speed between 20 m/s and 2405 m/s . If, however, the speed exceeds 2500 m/s , the nanospheres melt and fuse upon collisions and the theory fails to describe the impact.

Figure 4.7 exhibits time development of ξ_n . Upper and lower panels refer to the Model A and B, respectively. Open circles are the results of the MD simulation averaged over 100 samples and 10 samples for the Model A and B, respectively. Here, the incident angles are $\gamma = 0.05$ and $\gamma = 1.25$ for

the Model A and B, respectively. The solid lines are the solutions of the equation of motion Eq.(4.12). However, it should be noted that, in the case of the Model A, Eq.(4.12) is scaled by the LJ parameters and its form does not change even if the length L and time τ are rescaled to λL and $\lambda\tau$, respectively. Therefore, in Fig.4.7, we rescaled the length and time units of the theoretical curve for the Model A as $\lambda\sigma_{LJ}$ and $\lambda\sigma_{LJ}\sqrt{m/\epsilon}$ with $\lambda = 0.5$.

We wish to stress that our theoretical model, developed for nanoclusters, may be relevant for oblique collisions of macroscopic bodies, provided the re-orientation of the contact plane during the impact is not negligible. Relevance of the theory for collisions in wet granular systems is also expected [171, 172].

4.5 Conclusion

We perform a detailed study of the oblique impact of nanoclusters by means of Molecular Dynamics and theoretically. In simulations we use two models, a simplified one, based on the Lennard-Jones potential with a cohesive parameter and a realistic model for nanoclusters with covalently bonded atoms. We detect unexpected behavior of the normal restitution coefficient e , which becomes negative for large incident angles and explain this effect by the reorientation of the contact plane in the course of collision. We propose a modified definition of the restitution coefficient, \tilde{e} , which describes only the normal motion of particles, independently of their relative reorientation, and is always positive. A simple relation between e and \tilde{e} , that may be helpful for experiments is reported. We develop a theoretical model for an oblique impact, based on the continuum mechanics description of colliding particles, and demonstrate that theoretical predictions agree well with simulation results. Hence, we conclude that the macroscopic concepts of elasticity, surface tension and bulk viscosity are well applicable for nano-objects of a few hundreds atoms.

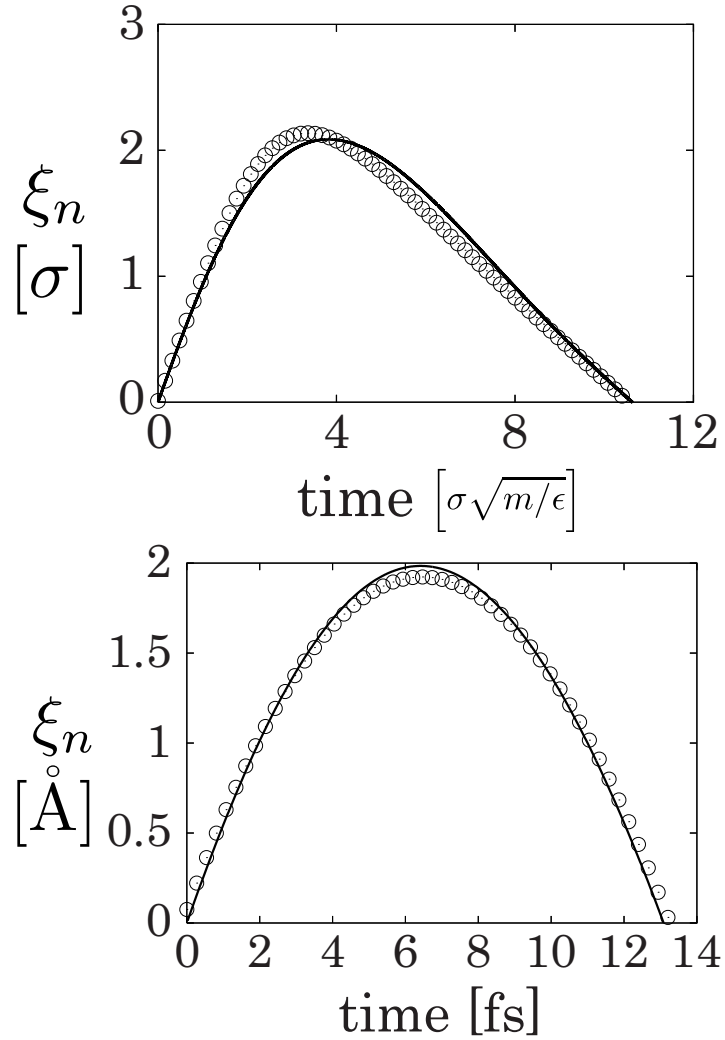


Figure 4.7: Time development of ξ_n . Upper and lower panels refer to the Model A and B, respectively. Open circles are the results of the MD simulation averaged over 100 samples and 10 samples for the Model A and B, respectively. Here, the incident angles are $\gamma = 0.05$ and $\gamma = 1.25$ for the Model A and B, respectively. The solid lines are the theoretical predictions, however, we rescaled the length and time units of the theoretical curve for the Model A as $\lambda\sigma_{LJ}$ and $\lambda\sigma_{LJ}\sqrt{m/\epsilon}$ with $\lambda = 0.5$.

Chapter 5

Summary

In Chapter 2, we find that deposited LJ nanoclusters consisting 32, 108, 255, 300, 500 and 862 atoms exhibit a transition from multilayered adsorption to monolayered adsorption at the critical incident speed, $V_{\text{imp}} = 3.3 \sqrt{\epsilon/m}$. From our simulation, we clarify that the deposited nanoclusters are perfectly wetting on the substrate above the critical incident speed. Employing the energy conservation law, we estimate the critical value of the incident speed at which the evaporation begins to occur during the impact. The estimated critical value, $V_{\text{imp}} = 1.7 \sqrt{\epsilon/m}$, exhibits good agreement with our simulation results. We also find that the scaled adsorption parameter is independent of the cluster size and is proportional to the square of the incident speed. These results also exhibit good agreement with the MD simulation results. We perform the Fourier analysis of the boundary shape of the adsorbed nanocluster and find that some modes becomes unstable for $3.0 \sqrt{\epsilon/m} < V_{\text{imp}} < 4.0 \sqrt{\epsilon/m}$. We also perform the MD simulation of A-C case and we find that the A cluster does not become a monolayer film on the C surface. Thus, we conclude that not only the incident speed, but also the strength of the interaction between the cluster and the substrate is important to form a monolayer film on a substrate. We also investigate the temperature dependence of deposited LJ nanoclusters and find that nanoclusters are stable if the temperature $T < T_C$ but the evaporation occurs if $T > T_C$. The morphology is almost independent of the temperature, and the binding energy and the orientational bond order parameter Q_6 increases as the temperature increases.

In Chapter 3, we perform the molecular dynamics simulation of the graphene sheet induced by a collision with an argon nanocluster, and the bending formation and the propagation of transverse deflection wave are observed. We find that the linear theory of the elasticity well explains the time evolution of the deflection of the graphene. In addition, we conclude that the actual thickness is much thinner than the diameter of a carbon atom from the analysis of the motion of the graphene. We also analyze the time evolution of the temperature profile, and find that the analysis based on the least dissipation principle reproduces our simulation result in the early stage of the impact.

In Chapter 4, we perform a detailed study of the oblique impact of nanoclusters by means of Molecular Dynamics and theoretically. In simulations, we use two models, a simplified one, based on the LJ potential with a cohesive parameter and a realistic model for nanoclusters with covalently bonded atoms. We detect unexpected behavior of the normal restitution coefficient e , which becomes negative for large incident angles and explain this effect by the reorientation of the contact plane in the course of collision. We propose a modified definition of the restitution coefficient, \tilde{e} , which describes only the normal motion of particles, independently of their relative reorientation, and is always positive. A simple relation between e and \tilde{e} , that may be helpful for experiments is reported. We develop a theoretical model for an oblique impact, based on the continuum mechanics description of colliding particles, and demonstrate that theoretical predictions agree well with simulation results. Hence, we conclude that the macroscopic concepts of elasticity, surface tension and bulk viscosity are well applicable for nano-objects of a few hundreds atoms.

Appendix A

Tersoff potential

The Tersoff potential is a bond-order potential used for the covalent bonding between two carbon (C) atoms or two silicon (Si) atoms [120–123]. Mota *et. al.* calculated the material parameters of the Tersoff potential to use the potential for silicon nitride and silicon hydride [124,125]. In this appendix, we explain how to use the Tersoff potential for the covalent bondings Si-Si, Si-H and H-H in the MD simulation.

A.1 Explicit form of the Tersoff potential

Interaction energy between atoms i and j is introduced as a sum of repulsive and attractive terms

$$V_{ij} = f_C(r_{ij}) [f_R(r_{ij}) + b_{ij}f_A(r_{ij})] , \quad (\text{A.1})$$

where r_{ij} is the distance between atoms i and j . In Eq.(A.1), f_R and f_A represent the repulsive and attractive interactions in the functional forms of Morse potential

$$f_R(r_{ij}) = A_{\alpha\beta} e^{-\lambda_{\alpha\beta} r_{ij}} , \quad (\text{A.2})$$

$$f_A(r_{ij}) = -B_{\alpha\beta} e^{-\mu_{\alpha\beta} r_{ij}} , \quad (\text{A.3})$$

and f_C is a cutoff function which decrease smoothly to zero between two distances $R_{\alpha\beta}$ and $S_{\alpha\beta}$

$$f_C(r_{ij}) = \begin{cases} 1 , & r_{ij} < R_{\alpha\beta} \\ \frac{1}{2} \left\{ 1 + \cos \frac{\pi(r_{ij}-R_{\alpha\beta})}{S_{\alpha\beta}-R_{\alpha\beta}} \right\} , & R_{\alpha\beta} < r_{ij} < S_{\alpha\beta} \\ 0 , & S_{\alpha\beta} < r_{ij} \end{cases} , \quad (\text{A.4})$$

where the subscripts α and β represent the species of atoms i and j , respectively.

In Eq.(A.1), b_{ij} represents the three body interaction of a triplet of three atoms i , j , and k which are arranged as Fig.A.1. The functional form of b_{ij} is

$$b_{ij} = \chi_{\alpha\beta} \left(1 + \beta_{\alpha}^{n_{\alpha}} \zeta_{ij}^{n_{\alpha}} \right)^{-\frac{1}{2n_{\alpha}}} , \quad (\text{A.5})$$

$$\zeta_{ij} = \sum_{k \neq i,j} f_C(r_{ik}) g(\theta_{ijk}) , \quad (\text{A.6})$$

$$g(\theta_{ijk}) = 1 + \left(\frac{c_{\alpha}}{d_{\alpha}} \right)^2 - \frac{c_{\alpha}^2}{d_{\alpha}^2 + (h_{\alpha} - \cos \theta_{ijk})^2} , \quad (\text{A.7})$$

where θ_{ijk} is the angle between ij and ik bonds, and $\chi_{\alpha\beta}$ is defined as

$$\chi_{\text{SiSi}} = \chi_{\text{HH}} = 1.0 , \quad (\text{A.8})$$

$$\chi_{\text{SiH}} = 0.78 . \quad (\text{A.9})$$

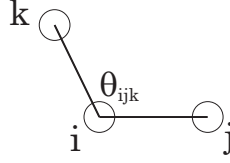


Figure A.1: The configuration of three atoms i , j , and k .

Table A.1: The list of material parameters for the Tersoff potential.

	Si	H
A (eV)	1.8308×10^3	86.7120
B (eV)	4.7118×10^2	43.5310
R (Å)	2.70	0.80
S (Å)	3.00	1.00
λ (Å ⁻¹)	2.4799	3.7879
μ (Å ⁻¹)	1.7322	1.9800
β	1.1000×10^{-6}	4.0000
n	7.8734×10^{-1}	1.00
c	1.0039×10^5	0.00
d	1.6217×10^1	1.00
h	-5.9825×10^{-1}	1.00

The parameters in Eqs.(A.2)-(A.4) are defined as

$$A_{\alpha\beta} = \sqrt{A_\alpha A_\beta}, \quad (\text{A.10})$$

$$B_{\alpha\beta} = \sqrt{B_\alpha B_\beta}, \quad (\text{A.11})$$

$$R_{\alpha\beta} = \sqrt{R_\alpha R_\beta}, \quad (\text{A.12})$$

$$S_{\alpha\beta} = \sqrt{S_\alpha S_\beta}, \quad (\text{A.13})$$

$$\lambda_{\alpha\beta} = \frac{\lambda_\alpha + \lambda_\beta}{2}, \quad (\text{A.14})$$

$$\mu_{\alpha\beta} = \frac{\mu_\alpha + \mu_\beta}{2}, \quad (\text{A.15})$$

$$(\text{A.16})$$

where the material parameters A_α , B_α , R_α , S_α , λ_α , μ_α , β_α , n_α , c_α , d_α , and h_α for silicon and hydrogen atoms ($\alpha = \text{Si}, \text{H}$) are listed in Table A.1.

A.2 Forces between interacting three atoms

The bond-order coefficient b_{ij} is generally asymmetry about i and j , i.e. $b_{ij} \neq b_{ji}$. However, Tersoff assumed in his article that b_{ij} and b_{ji} can be replaced by

$$b_{ij}^* = \frac{b_{ij} + b_{ji}}{2}. \quad (\text{A.17})$$

Let us introduce the positions of atoms i , j , and k as \mathbf{r}_i , \mathbf{r}_j , and \mathbf{r}_k , respectively. The forces acted

on the atoms i , j , and k are

$$\mathbf{F}_i = -\frac{\partial V_{ij}}{\partial \mathbf{r}_i} = -\left[(f_R + b_{ij}^* f_A) \frac{\partial f_C}{\partial r_{ij}} + \left(\frac{\partial f_R}{\partial r_{ij}} + b_{ij}^* \frac{\partial f_A}{\partial r_{ij}} \right) f_C \right] \frac{\mathbf{r}_{ij}}{r_{ij}} - f_C f_A \frac{\partial b_{ij}^*}{\partial \mathbf{r}_i}, \quad (\text{A.18})$$

$$\mathbf{F}_j = -\frac{\partial V_{ij}}{\partial \mathbf{r}_j} = \left[(f_R + b_{ij}^* f_A) \frac{\partial f_C}{\partial r_{ij}} + \left(\frac{\partial f_R}{\partial r_{ij}} + b_{ij}^* \frac{\partial f_A}{\partial r_{ij}} \right) f_C \right] \frac{\mathbf{r}_{ij}}{r_{ij}} - f_C f_A \frac{\partial b_{ij}^*}{\partial \mathbf{r}_j}, \quad (\text{A.19})$$

$$\mathbf{F}_k = -\frac{\partial V_{ij}}{\partial \mathbf{r}_k} = -f_C f_A \frac{\partial b_{ij}^*}{\partial \mathbf{r}_k}, \quad (\text{A.20})$$

respectively, where $\mathbf{r}_{ij} \equiv \mathbf{r}_i - \mathbf{r}_j$. In Eqs.(A.18)-(A.20), the derivatives of $f_R(r_{ij})$ and $f_A(r_{ij})$ are

$$\frac{\partial f_R(r_{ij})}{\partial r_{ij}} = -\lambda_{\alpha\beta} A e^{-\lambda_{\alpha\beta} r_{ij}}, \quad (\text{A.21})$$

$$\frac{\partial f_A(r_{ij})}{\partial r_{ij}} = \mu_{\alpha\beta} B e^{-\mu_{\alpha\beta} r_{ij}}, \quad (\text{A.22})$$

respectively. The derivatives of the cutoff function $f_C(r_{ij})$ is

$$\frac{\partial f_C(r_{ij})}{\partial r_{ij}} = \begin{cases} 0, & r_{ij} < R_{\alpha\beta} \\ -\frac{\pi}{2(S_{\alpha\beta} - R_{\alpha\beta})} \sin \frac{\pi(r_{ij} - R_{\alpha\beta})}{S_{\alpha\beta} - R_{\alpha\beta}}, & R_{\alpha\beta} < r_{ij} < S_{\alpha\beta} \\ 0. & S_{\alpha\beta} < r_{ij} \end{cases}, \quad (\text{A.23})$$

From Eq.(A.17),

$$\frac{\partial b_{ij}^*}{\partial \mathbf{r}_i} = \frac{1}{2} \left(\frac{\partial b_{ij}}{\partial \mathbf{r}_i} + \frac{\partial b_{ji}}{\partial \mathbf{r}_i} \right), \quad (\text{A.24})$$

where

$$\frac{\partial b_{ij}}{\partial \mathbf{r}_i} = -\frac{b_{ij} \beta_\alpha^{n_\alpha} \zeta_{ij}^{n_\alpha - 1}}{2(1 + \beta_\alpha^{n_\alpha} \zeta_{ij}^{n_\alpha})} \frac{\partial \zeta_{ij}}{\partial \mathbf{r}_i}. \quad (\text{A.25})$$

The derivatives of ζ_{ij} are

$$\frac{\partial \zeta_{ij}}{\partial \mathbf{r}_i} = \sum_{k \neq i, j} \left[g(\theta_{ijk}) \frac{\partial f_C(r_{ik})}{\partial r_{ik}} \frac{\mathbf{r}_{ik}}{r_{ik}} + f_C(r_{ik}) \frac{\partial g(\theta_{ijk})}{\partial \mathbf{r}_i} \right], \quad (\text{A.26})$$

$$\frac{\partial \zeta_{ij}}{\partial \mathbf{r}_j} = \sum_{k \neq i, j} f_C(r_{ik}) \frac{\partial g(\theta_{ijk})}{\partial \mathbf{r}_j}, \quad (\text{A.27})$$

$$\frac{\partial \zeta_{ij}}{\partial \mathbf{r}_k} = -g(\theta_{ijk}) \frac{\partial f_C(r_{ik})}{\partial r_{ik}} \frac{\mathbf{r}_{ik}}{r_{ik}} + f_C(r_{ik}) \frac{\partial g(\theta_{ijk})}{\partial \mathbf{r}_k}, \quad (\text{A.28})$$

and we can find that

$$\frac{\partial g(\theta_{ijk})}{\partial \mathbf{r}_i} = \frac{dg(\theta_{ijk})}{d(\cos \theta_{ijk})} \frac{\partial \cos \theta_{ijk}}{\partial \mathbf{r}_i} = \frac{2c_\alpha^2 (\cos \theta_{ijk} - h_\alpha)}{[d_\alpha^2 + (h_\alpha - \cos \theta_{ijk})^2]^2} \frac{\partial \cos \theta_{ijk}}{\partial \mathbf{r}_i}. \quad (\text{A.29})$$

Because

$$\cos \theta_{ijk} = \frac{r_{ij}^2 + r_{ik}^2 - r_{jk}^2}{2r_{ij}r_{ik}}, \quad (\text{A.30})$$

Eq.(A.29) can be calculated by using the following derivatives

$$\frac{\partial \cos \theta_{ijk}}{\partial \mathbf{r}_i} = \left(\frac{1}{r_{ik}} - \frac{\cos \theta_{ijk}}{r_{ij}} \right) \frac{\mathbf{r}_{ij}}{r_{ij}} + \left(\frac{1}{r_{ij}} - \frac{\cos \theta_{ijk}}{r_{ik}} \right) \frac{\mathbf{r}_{ik}}{r_{ik}}, \quad (\text{A.31})$$

$$\frac{\partial \cos \theta_{ijk}}{\partial \mathbf{r}_j} = \frac{\cos \theta_{ijk}}{r_{ij}} \frac{\mathbf{r}_{ij}}{r_{ij}} - \frac{1}{r_{ij}} \frac{\mathbf{r}_{ik}}{r_{ik}}, \quad (\text{A.32})$$

$$\frac{\partial \cos \theta_{ijk}}{\partial \mathbf{r}_k} = \frac{\cos \theta_{ijk}}{r_{ik}} \frac{\mathbf{r}_{ik}}{r_{ik}} - \frac{1}{r_{ik}} \frac{\mathbf{r}_{ij}}{r_{ij}}. \quad (\text{A.33})$$

Appendix B

Brenner potential

The Brenner potential is also a bond-order potential used for the covalent bonding between two carbon (C) atoms [126–129]. In this appendix, we follow Ref. [126] and explain how to use the Brenner potential for the covalent bondings C-C in the MD simulation.

B.1 Explicit form of the Brenner potential

Interaction energy between atoms i and j is introduced as a sum of repulsive and attractive terms

$$V_{ij} = f_C(r_{ij}) [f_R(r_{ij}) + b_{ij}f_A(r_{ij})], \quad (\text{B.1})$$

where r_{ij} is the distance between atoms i and j . In Eq.(B.1), f_R and f_A represent the repulsive and attractive interactions in the functional forms of Morse potential

$$f_R(r_{ij}) = \frac{A}{\beta - 1} e^{-\lambda \sqrt{2\beta}(r_{ij}-r_e)}, \quad (\text{B.2})$$

$$f_A(r_{ij}) = -\frac{\beta A}{\beta - 1} e^{-\lambda \sqrt{2\beta}(r_{ij}-r_e)}, \quad (\text{B.3})$$

and f_C is a cutoff function which decrease smoothly to zero between two distances R and S

$$f_C(r_{ij}) = \begin{cases} 1, & r_{ij} < R \\ \frac{1}{2} \left\{ 1 + \cos\left(\frac{\pi(r_{ij}-R)}{S-R}\right) \right\}, & R < r_{ij} < S \\ 0. & S < r_{ij} \end{cases} \quad (\text{B.4})$$

In Eq.(B.1), b_{ij} represents the three body interaction of a triplet of three atoms i , j , and k which are also arranged as Fig.A.1. The functional form of b_{ij} is

$$b_{ij} = \left(1 + \sum_{k \neq i, j} f_C(r_{ik}) g(\theta_{ijk}) \right)^{-\delta}, \quad (\text{B.5})$$

$$g(\theta_{ijk}) = \alpha_0 \left[1 + \left(\frac{c}{d} \right)^2 - \frac{c^2}{d^2 + (1 + \cos \theta_{ijk})^2} \right], \quad (\text{B.6})$$

where θ_{ijk} is the angle between ij and ik bonds. The material parameters are listed in Table B.1, and we also replace b_{ij} and b_{ji} by

$$b_{ij}^* = \frac{b_{ij} + b_{ji}}{2}. \quad (\text{B.7})$$

B.2 Forces between interacting three atoms

Let us introduce the positions of atoms i , j , and k as \mathbf{r}_i , \mathbf{r}_j , and \mathbf{r}_k , respectively. The forces acted on the atoms i , j , and k are

$$\mathbf{F}_i = -\frac{\partial V_{ij}}{\partial \mathbf{r}_i} = -\left[(f_R + b_{ij}^* f_A) \frac{\partial f_C}{\partial r_{ij}} + \left(\frac{\partial f_R}{\partial r_{ij}} + b_{ij}^* \frac{\partial f_A}{\partial r_{ij}} \right) f_C \right] \frac{\mathbf{r}_{ij}}{r_{ij}} - f_C f_A \frac{\partial b_{ij}^*}{\partial \mathbf{r}_i}, \quad (\text{B.8})$$

$$\mathbf{F}_j = -\frac{\partial V_{ij}}{\partial \mathbf{r}_j} = \left[(f_R + b_{ij}^* f_A) \frac{\partial f_C}{\partial r_{ij}} + \left(\frac{\partial f_R}{\partial r_{ij}} + b_{ij}^* \frac{\partial f_A}{\partial r_{ij}} \right) f_C \right] \frac{\mathbf{r}_{ij}}{r_{ij}} - f_C f_A \frac{\partial b_{ij}^*}{\partial \mathbf{r}_j}, \quad (\text{B.9})$$

$$\mathbf{F}_k = -\frac{\partial V_{ij}}{\partial \mathbf{r}_k} = -f_C f_A \frac{\partial b_{ij}^*}{\partial \mathbf{r}_k}, \quad (\text{B.10})$$

respectively, where $\mathbf{r}_{ij} \equiv \mathbf{r}_i - \mathbf{r}_j$. In Eqs.(B.8)-(B.10), the derivatives of $f_R(r_{ij})$ and $f_A(r_{ij})$ are

$$\frac{\partial f_R(r_{ij})}{\partial r_{ij}} = -B e^{-\lambda \sqrt{2\beta}(r_{ij}-r_e)}, \quad (\text{B.11})$$

$$\frac{\partial f_A(r_{ij})}{\partial r_{ij}} = B e^{-\lambda \sqrt{2\beta}(r_{ij}-r_e)}, \quad (\text{B.12})$$

where we introduced $B \equiv \lambda \sqrt{2\beta}A / (\beta - 1)$. The derivatives of the cutoff function $f_C(r_{ij})$ is

$$\frac{\partial f_C(r_{ij})}{\partial r_{ij}} = \begin{cases} 0, & r_{ij} < R \\ -\frac{\pi}{2(S-R)} \sin \frac{\pi(r_{ij}-R)}{S-R}, & R < r_{ij} < S \\ 0. & S < r_{ij} \end{cases} \quad (\text{B.13})$$

From Eq.(B.7),

$$\frac{\partial b_{ij}^*}{\partial \mathbf{r}_i} = \frac{1}{2} \left(\frac{\partial b_{ij}}{\partial \mathbf{r}_i} + \frac{\partial b_{ji}}{\partial \mathbf{r}_i} \right), \quad (\text{B.14})$$

where

$$\frac{\partial b_{ij}}{\partial \mathbf{r}_i} = -\frac{b_{ij} \delta}{1 + \zeta_{ij}} \frac{\partial \zeta_{ij}}{\partial \mathbf{r}_i}. \quad (\text{B.15})$$

In Eq.(B.15), we introduced $\zeta_{ij} \equiv \sum_{k \neq i, j} f_C(r_{ik}) g(\theta_{ijk})$. The derivatives of ζ_{ij} are

$$\frac{\partial \zeta_{ij}}{\partial \mathbf{r}_i} = \sum_{k \neq i, j} \left[g(\theta_{ijk}) \frac{\partial f_C(r_{ik})}{\partial r_{ik}} \frac{\mathbf{r}_{ik}}{r_{ik}} + f_C(r_{ik}) \frac{\partial g(\theta_{ijk})}{\partial \mathbf{r}_i} \right], \quad (\text{B.16})$$

$$\frac{\partial \zeta_{ij}}{\partial \mathbf{r}_j} = \sum_{k \neq i, j} f_C(r_{ik}) \frac{\partial g(\theta_{ijk})}{\partial \mathbf{r}_j}, \quad (\text{B.17})$$

$$\frac{\partial \zeta_{ij}}{\partial \mathbf{r}_k} = -g(\theta_{ijk}) \frac{\partial f_C(r_{ik})}{\partial r_{ik}} \frac{\mathbf{r}_{ik}}{r_{ik}} + f_C(r_{ik}) \frac{\partial g(\theta_{ijk})}{\partial \mathbf{r}_k}, \quad (\text{B.18})$$

and we can find that

$$\frac{\partial g(\theta_{ijk})}{\partial \mathbf{r}_i} = \frac{dg(\theta_{ijk})}{d(\cos \theta_{ijk})} \frac{\partial \cos \theta_{ijk}}{\partial \mathbf{r}_i} = \frac{2\alpha_0 c^2 (1 + \cos \theta_{ijk})}{[d^2 + (1 + \cos \theta_{ijk})^2]^2} \frac{\partial \cos \theta_{ijk}}{\partial \mathbf{r}_i}, \quad (\text{B.19})$$

which can be calculated by using Eqs.(A.31)-(A.33).

Table B.1: The list of material parameters for the Brenner potential.

$A(\text{eV})$	6.325	β	1.29
$r_e(\text{\AA})$	1.315	δ	0.80469
$R(\text{\AA})$	1.7	α_0	0.011304
$S(\text{\AA})$	2.0	c	19.0
$\lambda(\text{\AA}^{-1})$	1.5	d	2.5

Appendix C

Spin effect on the restitution coefficient of nanocluster

In this appendix, we derive the equation of motion Eq.(4.12) under *spin-less* approximation. We also explain how to calculate the angular displacement α and derive Eqs.(4.4), (4.5) and (4.13). Finally, we discuss the spin effect on the restitution coefficient of nanocluster.

C.1 *Spin-less* approximation

In the inertial frame, the angular momentum of the system is divided into two parts as

$$\begin{aligned}\mathbf{L} &= \mu r_{12}(\mathbf{n} \times \mathbf{v}_{12}) + I_1 \omega_1 + I_2 \omega_2 \\ &\equiv \mathbf{L}^{orbital} + \mathbf{L}^{spin},\end{aligned}\quad (\text{C.1})$$

where we introduce the orbital part $\mathbf{L}^{orbital} \equiv \mu r_{12}(\mathbf{n} \times \mathbf{v}_{12})$ and the spin part $\mathbf{L}^{spin} \equiv I_1 \omega_1 + I_2 \omega_2$ of the angular momentum. In Eq.(C.1), μ and \mathbf{n} are the reduced mass of cluster 1 and 2, and the normal vector projected from the center of mass (CM) of cluster 1 to the CM of cluster 2, respectively. r_{12} and \mathbf{v}_{12} are the distance between the CM of cluster 1 and the CM of cluster 2, and the translational relative velocity, respectively. I_α and ω_α are the moment of inertia and the angular velocity of cluster α . We assume that the rotation of cluster 1 and 2 occurs in the xy plane. This means that the angular momentum of the system only has the z -component. Thus, $\mathbf{L} = (0, 0, L_z)$, $\mathbf{L}^{orbital} = (0, 0, L_z^{orbital})$ and $\mathbf{L}^{spin} = (0, 0, L_z^{spin})$. If we introduce the angular velocity of \mathbf{n} as $\boldsymbol{\Omega} = (0, 0, \dot{\theta})$, we can find that

$$[\mathbf{n} \times \mathbf{v}_{12}]_z = r_{12} \dot{\theta}. \quad (\text{C.2})$$

Therefore, the orbital part of \mathbf{L} becomes

$$L_z^{orbital} = \mu r_{12}^2 \dot{\theta}. \quad (\text{C.3})$$

Before the collision, the cluster 1 moves to the cluster 2 with the incident velocity $\mathbf{v}_{12}(0) = (0, -V, 0)$, the angular velocities $\omega_1 = \omega_2 = \mathbf{0}$, and the incident angle γ . Thus, the angular momentum of the system before the collision is

$$\begin{aligned}\mathbf{L} &= \mu r_{12}[\mathbf{n}(0) \times \mathbf{v}_{12}(0)] \\ &= -\mu V d \sin \gamma \mathbf{e}_z,\end{aligned}\quad (\text{C.4})$$

here \mathbf{e}_z is the unit vector projected to the z -axis. From the conservation law of the angular momentum of the system,

$$L_z = -\mu V d \sin \gamma. \quad (\text{C.5})$$

Therefore, from Eqs.(C.1), (C.3) and (C.5), the angular velocity $\dot{\theta}$ becomes

$$\begin{aligned}\dot{\theta} &= \frac{L_z - L_z^{spin}}{\mu r_{12}^2} \\ &= -\frac{\mu V d \sin \gamma + L_z^{spin}}{\mu r_{12}^2}.\end{aligned}\quad (\text{C.6})$$

In the non-inertial frame, the equation of motion is

$$\mu \frac{d'}{dt} v'_n = F_n + F_I, \quad (\text{C.7})$$

where d'/dt represents the time derivative in the non-inertial frame, and $v'_n = d' r_{12}/dt$. The normal force F_n acts between the CM of cluster 1 and the CM of cluster 2, and the inertial force for the normal motion F_I is given by

$$F_I = 2\mu \mathbf{v}_{12} \cdot \dot{\mathbf{n}}(t) - \mu r_{12} |\dot{\mathbf{n}}(t)|^2. \quad (\text{C.8})$$

Because $|\dot{\mathbf{n}}| = |\boldsymbol{\Omega} \times \mathbf{n}| = \dot{\theta}$ and

$$\begin{aligned}\mathbf{v}_{12} \cdot \dot{\mathbf{n}} &= \mathbf{v}_{12} \cdot [\boldsymbol{\Omega} \times \mathbf{n}] \\ &= \boldsymbol{\Omega} \cdot [\mathbf{n} \times \mathbf{v}_{12}] \\ &= r_{12} \dot{\theta}^2,\end{aligned}\quad (\text{C.9})$$

we find

$$F_I = 2\mu r_{12} \dot{\theta}^2 - \mu r_{12} \dot{\theta}^2 = \mu r_{12} \dot{\theta}^2. \quad (\text{C.10})$$

Thus, Eq. (C.7) becomes

$$\mu \frac{d'}{dt} v'_n = F_n + \mu r_{12} \dot{\theta}^2. \quad (\text{C.11})$$

If we neglect L_z^{spin} in Eq. (C.6), which we call *spin-less* approximation, the angular velocity of \mathbf{n} is given by

$$\dot{\theta} = -\frac{Vd}{r_{12}^2} \sin \gamma. \quad (\text{C.12})$$

Because the normal compression is defined as $\xi_n = d - r_{12}$, i.e. $d' v'_n/dt = -d'^2 \xi_n/dt^2$, and we adopt the model for dissipative particles, i.e. $F_n = F_H - F_B + F_D$, Eq.(C.11) gives the equation of motion of ξ_n

$$\mu \frac{d'^2}{dt^2} \xi_n + F_H - F_B + F_D + \frac{\mu V^2 d^2}{(d - \xi_n)^3} \sin^2 \gamma = 0, \quad (\text{C.13})$$

which is Eq.(4.12) in Chap.4.

C.2 Angular displacement α

Because of $\dot{\mathbf{n}} = \boldsymbol{\Omega} \times \mathbf{n}$, we can find the time evolution of $\mathbf{n}(t) = (n_x, n_y, n_z)$ by solving the following equations.

$$\dot{n}_x = -\dot{\theta} n_y = \frac{Vd}{r_{12}^2} \sin \gamma n_y, \quad (\text{C.14})$$

$$\dot{n}_y = \dot{\theta} n_x = -\frac{Vd}{r_{12}^2} \sin \gamma n_x, \quad (\text{C.15})$$

$$\dot{n}_z = 0. \quad (\text{C.16})$$

Here, the time evolution of $r_{12} = d - \xi_n$ is found by solving Eq.(C.13). Therefore, the angular displacement α

$$\cos \alpha = \mathbf{n}(0) \cdot \mathbf{n}(t_c) \quad (\text{C.17})$$

can be calculated and the results are displayed in Fig.4.6.

C.3 Derivations of Eqs.(4.4), (4.5) and (4.13)

The inner products of $\mathbf{g}(0)$, $\mathbf{g}(t_c)$ and $\mathbf{n}(0)$ are

$$\mathbf{g}(0) \cdot \mathbf{n}(0) = -\dot{\xi}_n(0), \quad (\text{C.18})$$

$$\mathbf{g}(t_c) \cdot \mathbf{n}(0) = -\dot{\xi}_n(t_c) (\mathbf{n}(t_c) \cdot \mathbf{n}(0)) + d (\dot{\mathbf{n}}(t_c) \cdot \mathbf{n}(0)). \quad (\text{C.19})$$

The angular displacement at time t is

$$\cos \alpha(t) = \mathbf{n}(0) \cdot \mathbf{n}(t), \quad (\text{C.20})$$

and the time derivative of $\alpha(t)$ is

$$-\dot{\alpha}(t) \sin \alpha(t) = \mathbf{n}(0) \cdot \dot{\mathbf{n}}(t). \quad (\text{C.21})$$

Then, the restitution coefficient in the inertial frame is

$$\begin{aligned} e &= -\frac{\mathbf{g}(t_c) \cdot \mathbf{n}(0)}{\mathbf{g}(0) \cdot \mathbf{n}(0)} \\ &= -\frac{\dot{\xi}_n(t_c)}{\dot{\xi}_n(0)} \cos \alpha - \frac{d \sin \alpha \dot{\alpha}(t_c)}{\dot{\xi}_n(0)}, \end{aligned} \quad (\text{C.22})$$

where we omit the argument of $\alpha(t_c) \equiv \alpha$. Because $\dot{\xi}_n(t_c)/\dot{\xi}_n(0)$ is always negative and $\dot{\xi}_n(0) = V \cos \gamma$, Eq.(C.22) is rewritten as

$$e = \left| \frac{\dot{\xi}_n(t_c)}{\dot{\xi}_n(0)} \right| \cos \alpha - \frac{d \sin \alpha \dot{\alpha}(t_c)}{V \cos \gamma}, \quad (\text{C.23})$$

which is Eq.(4.4) in Chap.4. In the same way,

$$\tilde{e} = -\frac{\mathbf{g}(t_c) \cdot \mathbf{n}(t_c)}{\mathbf{g}(0) \cdot \mathbf{n}(0)} = \left| \frac{\dot{\xi}_n(t_c)}{\dot{\xi}_n(0)} \right|, \quad (\text{C.24})$$

which is Eq.(4.5) in Chap.4. Because $\dot{\alpha}(t) = -\dot{\theta} = Vd \sin \gamma / r_{12}^2$,

$$\dot{\alpha}(t_c) = \frac{V \sin \gamma}{d}. \quad (\text{C.25})$$

From Eqs. (C.23)-(C.25),

$$\begin{aligned} e &= \tilde{e} \cos \alpha - \frac{d \sin \alpha}{V \cos \gamma} \frac{V \sin \gamma}{d} \\ &= \tilde{e} \cos \alpha - \tan \gamma \sin \alpha, \end{aligned} \quad (\text{C.26})$$

which is Eq.(4.13) in Chap.4.

C.4 Spin effect on the restitution coefficient

If we use the *spin-less* approximation, the dissipative constants are $\eta = 0.65\sigma \sqrt{m/\epsilon}$ and 1.62 fs for models A and B, respectively. Figure C.1 displays the results of the restitution coefficient \tilde{e} under the *spin-less* approximation and the results of \tilde{e} with L_z^{spin} which is measured in the MD simulation. Upper and lower panels refer to the model A and B, respectively. When the MD simulation result of L_z^{spin} is introduced, \tilde{e} for the model A is almost same with the result of *spin-less* approximation. However, \tilde{e} for the model B becomes larger than the case of *spin-less* approximation.

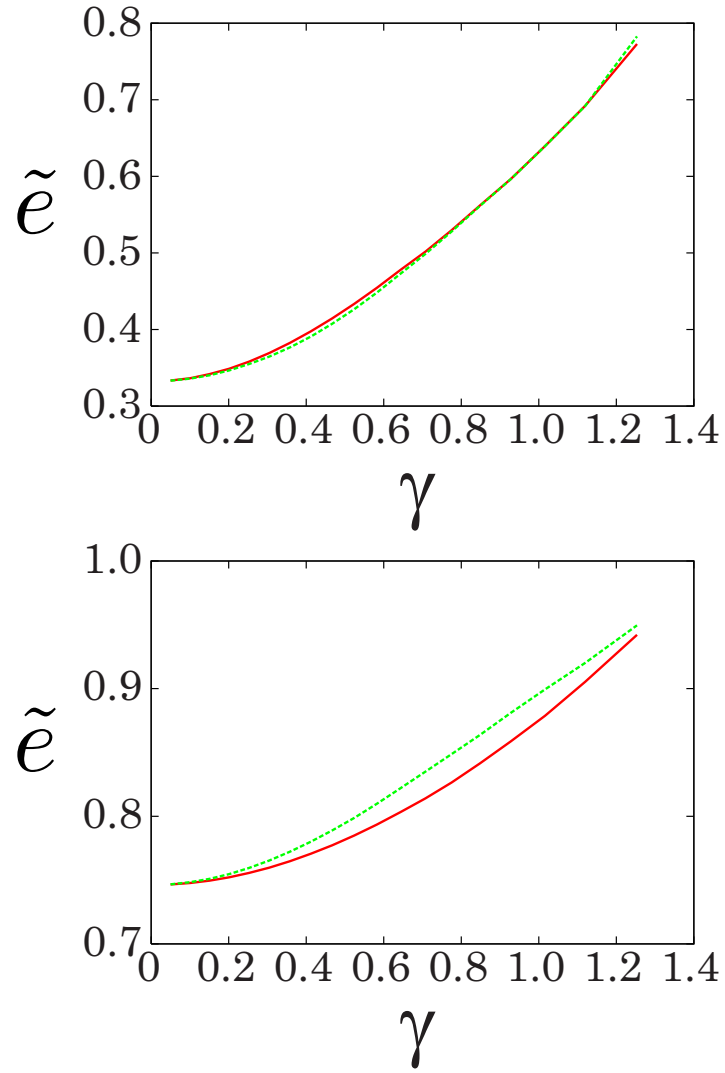


Figure C.1: The results of the restitution coefficient \tilde{e} under the *spin-less* approximation (red solid lines) and the results of \tilde{e} with L_z^{spin} which is measured in the MD simulation (green broken lines). Upper and lower panels refer to the model A and B, respectively.

Appendix D

Elastic modulus and surface tension of a nanocluster

D.1 Elastic modulus

If an elastic body is deformed, the variation of free energy per unit volume is represented as

$$\Delta F = \frac{K}{2} u_{ll}^2 + \lambda \left(u_{ik} - \frac{1}{3} \delta_{ik} u_{ll} \right)^2, \quad (\text{D.1})$$

where u_{ik} , K and λ are the strain tensor, the compressibility and the shear rate, respectively. In this section, we explain how to measure Young's modulus Y and the Poisson ratio ν of nanocluster, which are related to K and λ by

$$Y = \frac{9\lambda K}{3K + \lambda}, \quad (\text{D.2})$$

$$\nu = \frac{1}{2} \frac{3K - 2\lambda}{3K + \lambda}, \quad (\text{D.3})$$

respectively.

D.1.1 Isotropic compression

To measure the compressibility K of nanocluster, we consider isotropic compression. At first, we put the center of mass of nanocluster onto the origin. If we give the displacement $(u_x, u_y, u_z) = (ax, ay, az)$ to each atom in nanocluster with the deformation rate a , the components of the strain tensor are given by

$$u_{xx} = \frac{\partial u_x}{\partial x} = a, \quad (\text{D.4})$$

$$u_{yy} = \frac{\partial u_y}{\partial y} = a, \quad (\text{D.5})$$

$$u_{zz} = \frac{\partial u_z}{\partial z} = a, \quad (\text{D.6})$$

and $u_{ik} = 0$ ($i \neq k$), respectively. In this case,

$$u_{ll}^2 = (u_{xx} + u_{yy} + u_{zz})^2 = 9a^2, \quad (\text{D.7})$$

$$\left(u_{ik} - \frac{1}{3} \delta_{ik} u_{ll} \right)^2 = 0, \quad (\text{D.8})$$

where we use $\delta_{ll} = 3$. Therefore, from Eq. (D.1), the compressibility K of nanocluster is given by

$$K = \frac{2\Delta F}{9a^2}. \quad (\text{D.9})$$

If we assume the deformation of nanocluster is taken place adiabatically, the variation of free energy equals the variation of internal energy ΔE , which is the change of the potential energy of nanocluster. In Chap.4, we measure ΔE in another MD simulation and find K of nanocluster from $K = 2\Delta E/9a^2$.

D.1.2 Shearing deformation

To measure the shear rate λ of nanocluster, we consider shear deformation. We also put the center of mass of nanocluster onto the origin and give the displacement $(u_x, u_y, u_z) = (ay, 0, 0)$ to each atom in nanocluster with the deformation rate a . In this case, the components of strain tensor u_{xy} and u_{yx} are given by

$$u_{xy} = u_{yx} = \frac{1}{2} \left(\frac{\partial u_x}{\partial y} + \frac{\partial u_y}{\partial x} \right) = \frac{a}{2}, \quad (\text{D.10})$$

and other components are zero. Thus,

$$u_{ll}^2 = 0, \quad (\text{D.11})$$

$$\left(u_{ik} - \frac{1}{3} \delta_{ik} u_{ll} \right)^2 = \frac{a^2}{2}. \quad (\text{D.12})$$

Therefore, from Eq.(D.1), the shear rate λ of nanocluster is given by

$$\lambda = \frac{2\Delta F}{a^2}. \quad (\text{D.13})$$

In Chap.4, we also assume the deformation is adiabatic. Then, we measure ΔE in another MD simulation and find λ of nanocluster from $\lambda = 2\Delta E/a^2$.

In the same way, we also give the displacements $(u_x, u_y, u_z) = (az, 0, 0)$, $(u_x, u_y, u_z) = (0, az, 0)$, $(u_x, u_y, u_z) = (0, ax, 0)$, $(u_x, u_y, u_z) = (0, 0, ax)$ and $(u_x, u_y, u_z) = (0, 0, ay)$ to nanocluster, and measure λ from $\lambda = 2\Delta E/a^2$. Finally, we determine λ as the averaged value of these six measurements.

D.2 Surface tension

D.2.1 Model of interacting two spheres

The surface tension σ is defined as

$$\sigma = \frac{E(l_{eq})}{2}, \quad (\text{D.14})$$

where E and l_{eq} are the interaction energy and the equilibrium distance between two nanoclusters, respectively. The interaction energy is represented by

$$E = \rho^2 \int_{V_1} d\mathbf{r}_1 \int_{V_2} d\mathbf{r}_2 \phi_{12}, \quad (\text{D.15})$$

where V_α ($\alpha = 1, 2$) is the volume of nanocluster α , and ϕ_{12} is the interatomic two body potential. In Eq.(D.15), we assume the number density of atoms in nanocluster ρ is constant.

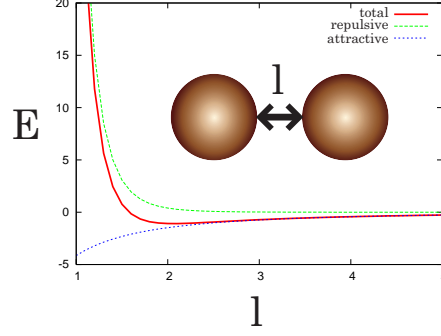


Figure D.1: The red solid, the green broken, and the blue broken lines are respectively the interaction energy E , the repulsive energy E_{rep} , and the attractive energy E_{att} as the functions of the distance l . Here, the radius of the interacting two nanocluster is $5.23\sigma_{LJ}$.

In the case of *Model A* in Chap.4, the interatomic potential ϕ_{12} is the modified LJ potential with the cohesive parameter $C = 0.2$. The repulsive and attractive parts of $\phi_{12}(r) = \phi_{rep}(r) + \phi_{att}(r)$ are

$$\phi_{rep}(r) = 4\epsilon \left(\frac{\sigma_{LJ}}{r} \right)^{12}, \quad (\text{D.16})$$

$$\phi_{att}(r) = -4\epsilon C \left(\frac{\sigma_{LJ}}{r} \right)^6, \quad (\text{D.17})$$

respectively. Thus, the interaction energy $E = E_{rep} + E_{att}$ is represented by

$$E_{rep} = 4\rho^2 \epsilon \sigma_{LJ}^{12} \int_{V_1} d\mathbf{r}_1 \int_{V_2} d\mathbf{r}_2 \frac{1}{r^{12}}, \quad (\text{D.18})$$

$$E_{att} = -4\rho^2 \epsilon \sigma_{LJ}^6 C \int_{V_1} d\mathbf{r}_1 \int_{V_2} d\mathbf{r}_2 \frac{1}{r^6}. \quad (\text{D.19})$$

If we assume the interacting two nanoclusters are spheres with radii R_1 and R_2 , Eqs.(D.18) and (D.19) can be integrated by the method of Ref. [173], and we find

$$E_{rep} = \frac{\pi^2 \epsilon \sigma_{LJ}^{12} C}{540D} \int_{D-R_2}^{D+R_2} dr \left[\frac{r+9R_1}{(r+R_1)^9} - \frac{r-9R_1}{(r-R_1)^9} \right], \quad (\text{D.20})$$

$$E_{att} = -\frac{2\pi^2 \rho^2 \epsilon \sigma_{LJ}^6 C}{3} \left[\frac{2R_1 R_2}{D^2 - (R_1 + R_2)^2} + \frac{2R_1 R_2}{D^2 - (R_1 - R_2)^2} + \ln \frac{D^2 - (R_1 + R_2)^2}{D^2 - (R_1 - R_2)^2} \right], \quad (\text{D.21})$$

where $D \equiv R_1 + R_2 + l$ and l is the distance between two surfaces of nanocluster (see Fig.D.1). Although Eq.(D.20) can be integrated analytically, the result is too complicated to write this appendix. In our MD simulation, the radius of nanocluster is $R_1 = R_2 = 5.23\sigma_{LJ}$.

Figure D.1 shows the results of the interaction energy E , the repulsive energy E_{rep} and the attractive energy E_{att} as the functions of the distance l , respectively. From this result, the equilibrium distance is $l_{eq} = 2.1\sigma_{LJ}$ and the surface tension σ is estimated as

$$\sigma = \frac{E(l_{eq})}{2} \approx 0.54287\epsilon / \sigma_{LJ}^2. \quad (\text{D.22})$$

Because Eq.(D.15) is represented by the two body interatomic potential ϕ_{12} , we can not use Eq.(D.15) in the case of H-passivated Si nanoclusters (*Model B* in Chap.4) where we use the Tersoff potential with the three body interaction terms.

D.2.2 Model of compressed two spheres

If we follow the JKR theory [81], the surface tension σ is defined as

$$\sigma = \frac{E(\xi_n)}{2\pi a^2}, \quad (\text{D.23})$$

where $E(\xi_n)$, ξ_n and a are the interaction energy, the normal compression and the contact radius of colliding two nanoclusters, respectively. If $D_0/R \ll 1$, where $D_0 = 2 \cdot 2^{1/6} \sigma_{LJ}$ and R is the radius of nanocluster, Eq.(D.23) can be reduced to

$$\sigma = \frac{A_H}{24\pi D_0^2}, \quad (\text{D.24})$$

where A_H is the Hamaker constant.

In the case of *Model A* in Chap.4, we can find

$$A_H = 4\pi^2 C \rho^2 \epsilon \sigma_{LJ}^6, \quad (\text{D.25})$$

and calculate the surface tension σ analytically. However, in the case of *Model B* in Chap.4, we can not calculate A_H analytically. Therefore, we measure $E(\xi_n)$ and a by another MD simulation and find σ of H-passivated Si nanocluster from Eq.(D.23).

Bibliography

- [1] M. Terrones *et. al.* Nano Today **5** (2010), 351.
- [2] G.D. Scholes and G. Rumbles, Nature Materials. **5** (2006), 683.
- [3] H. Dai, Acc. Chem. Res. **35** (2002), 1035.
- [4] T. L. Hill, *Thermodynamics of Small Systems*, Parts I and II (Benjamin, Amsterdam, 1964).
- [5] B.M. Smirnov and R.S. Berry, *Phase Transitions of Simple Systems* (Springer-Verlag, Berlin and Heidelberg, 2007).
- [6] F. Baletto and R. Ferrando, Rev. Mod. Phys. **77** (2005), 371.
- [7] R.S. Berry and B.M. Smirnov, Physics Uspekhi **48** (2005), 345.
- [8] A. Rytkönen, S. Valkealahti and M. Manninen, J. Chem. Phys. **106** (1997), 1888.
- [9] A. Rytkönen, S. Valkealahti and M. Manninen, J. Chem. Phys. **108** (1998), 5826.
- [10] C.L. Cleveland, U. Landman, T.G. Schaaff, M.N. Shafigullin, P.W. Stephens and R.L. Whetten, Phys. Rev. Lett. **79** (1997), 1873.
- [11] H.-S. Nam, N.M. Hwang, B.D. Yu and J.-K. Yoon, Phys. Rev. Lett. **30** (2002), 275502.
- [12] K. Koga, T. Ikeshoji and K. Sugawara, Phys. Rev. Lett. **92** (2004), 115507.
- [13] C.-L. Kuo and P. Clancy, J. Phys. Chem. B **109** (2005), 13743.
- [14] M.Á G.-Pinilla *et. al.* J. Phys. Chem. C **112** (2008), 13492.
- [15] E.G. Noya, J.P.K. Doye and F. Calvo, Phys. Rev. B **73** (2006), 125407.
- [16] F. Baletto, C. Mottet and R. Ferrando, Chem. Phys. Lett. **354** (2002), 82.
- [17] Y. Qi *et. al.* J. Chem. Phys. **115** (2001), 385.
- [18] J.P.K. Doye and D.J. Wales, J. Chem. Phys. **102** (1995), 9659.
- [19] J.P.K. Doye, D.J. Wales and R.S. Berry, J. Chem. Phys. **103** (1995), 4234.
- [20] J.P.K. Doye and D.J. Wales, Phys. Rev. Lett. **80** (1998), 1357.
- [21] J.P.K. Doye, D.J. Wales and M.A. Miller, J. Chem. Phys. **109** (1998), 8143.
- [22] J.P.K. Doye and F. Calvo, Phys. Rev. Lett. **86** (2001), 3570.
- [23] J.P.K. Doye, Phys. Rev. Lett. **88** (2002), 238701.
- [24] J.P.K. Doye and D.J. Wales, J. Chem. Phys. **116** (2002), 3777.
- [25] J.P.K. Doye and F. Calvo, J. Chem. Phys. **116** (2002), 8307.
- [26] F. Calvo, J.P.K. Doye and D.J. Wales, Chem. Phys. Lett. **366** (2002), 176.
- [27] F. Calvo and J.P.K. Doye, Phys. Rev. B **69** (2004), 125414.
- [28] J.P.K. Doye and C.P. Massen, J. Chem. Phys. **122** (2005), 084105.
- [29] E.G. Noya and J.P.K. Doye, J. Chem. Phys. **124** (2006), 104503.

- [30] N.V. Krainyukova, Eur. Phys. J. D **43** (2007), 45.
- [31] W. Lechner and C. Dellago, J. Chem. Phys. **129** (2008), 114707.
- [32] D. J. Wales, *Energy Landscapes with Applications to Clusters, Biomolecules and Glasses* (Cambridge University, Cambridge, England, 2003).
- [33] Y. Imry, Phys. Rev. B **21** (1980), 2042.
- [34] P. Labastie and R.L. Whetten, Phys. Rev. Lett. **65** (1990), 1567.
- [35] M. Schmidt, R. Kusche, B. von Issendorff and H. Haberland, Nature **393** (1998), 238.
- [36] M. Schmidt, R. Kusche, T. Hippler, J. Donges, W. Kronmüller, B. von Issendorff and H. Haberland, Phys. Rev. Lett. **86** (2001), 1191.
- [37] W.A. de Heer, Rev. Mod. Phys. **65** (1993), 611.
- [38] C. Binns, Surf. Sci. Rep. **44** (2001), 1.
- [39] K. Wegner, P. Piseri, H.V. Tafreshi and P. Milani, J. Phys. D: Appl. Phys. **39** (2006), R439.
- [40] O.G. Danylchenko, S.I. Kovalenko and V.N. Samovarov, Low Temp. Phys. **30** (2004), 743.
- [41] W. Polak and A. Patrykiewicz, Phys. Rev. B **67** (2003), 115402.
- [42] N. Nishio, J. Koga, T. Yamaguchi and F. Yonezawa, J. Phys. Soc. Jpn. **73** (2004), 627.
- [43] W. Polak, Eur. Phys. J. D **40** (2006), 231.
- [44] W. Polak, Phys. Rev. E **77** (2008), 031404.
- [45] V. V. Hoang and T. Odagaki, Phys. Rev. B **77** (2008), 125434.
- [46] T. Bachelors and R. Schäfer, Chem. Phys. Lett. **324** (2000), 365.
- [47] M.O. Watanabe, N. Uchida and T. Kanayama, Phys. Rev. B **61** (2000), 7219.
- [48] W.W. Gerberich *et. al.* J. Mech. Phys. Solids **51** (2003), 979.
- [49] S.L. Girshick and J. Hafiz, J. Phys. D: Appl. Phys. **40** (2007), 2354.
- [50] P. Jensen, Rev. Mod. Phys. **71** (1999), 1695.
- [51] I. Yamada, H. Inokawa and T. Takagi, J. Appl. Phys. **56** (1984), 2746.
- [52] I. Yamada, G. H. Takaoka, H. Usui, F. Satoh, Y. Itoh, K. Yamashita, S. Kitamoto, Y. Namba, Y. Hashimoto, Y. Maeyama and K. Machida, Nucl. Instrum. Methods Phys. Res. B **59** (1991), 216.
- [53] T. Takagi, Z. Phys. D **3** (1986), 271.
- [54] X. Kang, L. T. Wille, H. Dreyssé and J. Eugène, Nucl. Instrum. Methods Phys. Res. B **122** (1997), 339.
- [55] K. Nordlund, T. T. Järvi, K. Meinander and J. Samela, Appl. Phys. A **91** (2008), 561.
- [56] C.L. Cleveland and U. Landman, Science **257** (1992), 355.
- [57] Y. Guoqing *et. al.* Nucl. Inst. Meth. Phys. Res. B **135** (1998), 382.

- [58] K. Koga and K. Sugawara, *Surf. Sci.* **529** (2003), 23.
- [59] K-H. Müller, *J. Appl. Phys.* **61** (1987), 2516.
- [60] Y. Yamamura, *Nucl. Instrum. Methods Phys. Res. B* **45** (1990), 707.
- [61] H. Haberland, Z. Insepov and M. Moseler, *Phys. Rev. B* **51** (1995), 11061.
- [62] Y. Yamaguchi and J. Gspann, *Phys. Rev. B* **66** (2002), 155408.
- [63] R. Krämer, Y. Yamaguchi and J. Gspann, *Surf. Interface. Anal.* **36** (2004), 148.
- [64] A. Terasaki, *J. Phys. Chem. A* **111** (2007), 32.
- [65] S. Bouneau, A. Brunelle, S. Della-Negra, J. Depauw, D. Jacquet, Y. LeBeyec, M. Pautrat, M. Fallavier, J. C. Poizat and H. H. Andersen, *Phys. Rev. B* **65** (2002), 144106.
- [66] J. Samela, J. Kotakoshi, K. Nordlund and J. Keinonen, *Nucl. Instrum. Methods Phys. Res. B* **239** (2005), 331.
- [67] M. Moseler, O. Rattunde, J. Nordiek and H. Haberland, *Nucl. Instrum. Methods Phys. Res. B* **164-165** (2000), 522.
- [68] A. Tomsic, P. U. Andersson, N. Markovic, W. Piskorz, M. Svanberg and J. B. C. Pettersson, *J. Chem. Phys.* **115** (2001), 10509.
- [69] T. T. Järvi, A. Kuronen, K. Meinander, K. Nordlund and K. Albe, *Phys. Rev. B* **75** (2007), 115422.
- [70] A. Awasthi, S. C. Hendy, P. Zoontjens and S. A. Brown, *Phys. Rev. Lett.* **97** (2006), 186103.
- [71] A. Awasthi, S. C. Hendy, P. Zoontjens, S. A. Brown and F. Natali, *Phys. Rev. B* **76** (2007), 115437.
- [72] M. Suri and T. Dumitrică, *Phys. Rev. B* **78** (2008), 081405(R).
- [73] A. Castellanos, *Adv. Phys.* **54** (2005), 263.
- [74] J. Tomas, *Chem. Eng. Sci.* **62** (2007), 1997.
- [75] J. Tomas, *Chem. Eng. Sci.* **62** (2007), 5925.
- [76] R. Tykhoniuk, J. Tomas, S. Luding, M. Kappl, L. Heim and H.-J. Butt, *Chem. Eng. Sci.* **62** (2007), 2843.
- [77] A. Bertram and J. Tomas, *Micro-Macro-Interactions in Structured Media and Particle Systems* (Springer-Verlag, Berlin and Heidelberg, 2008).
- [78] H. Hertz, *J. reine und angewandte Mathematik*, **92** (1882), 156.
- [79] K.L. Johnson, *Contact mechanics* (Cambridge University Press, The Edinburgh Building, Cambridge CB2 2RU, UK, 1985).
- [80] D.A. Hills, D. Nowell and A. Sackfield, *Mechanics of Elastic Contact* (Butterworth-Heinemann Ltd, Linacre House, Jordan Hill, Oxford OX2 8DP, UK, 1993).
- [81] K. L. Johnson, K. Kendall, and A. D. Roberts, *Proc. R. Soc. London* **324** (1971), 301.

- [82] N. V. Brilliantov and T. Pöschel, *Kinetic Theory of Granular Gases* (Oxford University Press, Oxford, 2004).
- [83] A. Domenech, *Int. J. Mech. Sci.* **50** (2008), 752.
- [84] F.G. Bridges and A. Hatzes and D.N.C. Lin, *Nature (London)* **309** (1984), 333.
- [85] G. Kuwabara and K. Kono, *Jpn. J. Appl. Phys.* **26** (1987), 1230
- [86] N. V. Brilliantov, F. Spahn, J. M. Hertzsch, and T. Pöschel, *Phys. Rev. E* **53** (1996), 5382.
- [87] N. V. Brilliantov, N. Albers, F. Spahn, and T. Pöschel, *Phys. Rev. E* **76** (2007), 051302.
- [88] M.Y. Louge and M.E. Adams, *Phys. Rev. E* **65** (2002), 021303.
- [89] H. Kuninaka and H. Hayakawa, *Phys. Rev. Lett.* **93** (2004), 154301.
- [90] H. Hayakawa and H. Kuninaka, *Phase Transit.* **77** (2004), 889.
- [91] M. Kalweit and D. Drikakis, *J. Comput. Theor. Nanosci.* **1** (2004), 367.
- [92] M. Kalweit and D. Drikakis, *Phys. Rev. B* **74** (2006), 235415.
- [93] H. Kuninaka and H. Hayakawa, *Phys. Rev. E* **79** (2009), 031309.
- [94] A. Awasthi, S.C. Hendy, P. Zoontjens and S.A. Brown, *Phys. Rev. Lett.* **97** (2006), 186103.
- [95] A.I. Ayes, S.A. Brown, A. Awasthi, S.C. Hendy, P.Y. Convers, and K. Nichol, *Phys. Rev. B* **81** (2010), 195422.
- [96] C. Bostedt *et. al.* *Phys. Rev. Lett.* **100** (2008), 133401.
- [97] A. K. Geim and K. S. Novoselov, *Nature materials* **6** (2007), 183.
- [98] M. H. Gass, U. Bangert, A. L. Bleloch, P. Wang, R. R. Nair, and A. K. Geim, *Nature nanotechnology* **3** (2008), 676.
- [99] D. Garcia-Sanchez, A. M. van der Zande, A. S. Paulo, B. Lassagne, P. L. McEuen, and A. Bachtold, *Nano letters* **8** (2008), 1399.
- [100] J. C. Meyer, A. K. Geim, M. I. Katsnelson, K. S. Novoselov, T. J. Booth, and S. Roth, *Nature* **446** (2007), 60.
- [101] J. S. Bunch, A. M. van der Zande, S. S. Verbridge, Ian W. Frank, D. M. Tanenbaum, J. M. Parpia, H. G. Craighead, and P. L. McEuen, *Science* **315** (2007), 490.
- [102] Y. Huang, J. Wu, and K. C. Hwang, *Phys. Rev. B* **74** (2006), 245413.
- [103] C. D. Reddy, S. Rajendran, and K. M. Liew, *Nanotechnology* **17** (2006), 864.
- [104] Q. Lu, M. Arroyo, and R. Huang, *J. Phys. D : Appl. Phys.* **42** (2009), 102002.
- [105] J. W. Jiang, J. S. Wang, and B. Li, *Phys. Rev. B* **80** (2009), 113405.
- [106] P. Liu and Y.W. Zhang, *Appl. Phys. Lett.* **94** (2009), 231912.
- [107] J. Zhou and R. Huang, *J. Mech. Phys. Solids* **56** (2008), 1609.
- [108] B. I. Yakobson, C. J. Brabec, and J. Bernholc, *Phys. Rev. Lett.* **76** (1996), 2511.

- [109] C.Q. Ru, Phys. Rev. B **62** (2000), 9973.
- [110] M. Arroyo and T. Belytschko, Phys. Rev. B **69** (2004), 115415.
- [111] C. Tang, W. Guo and C. Chen, Phys. Rev. Lett. **100** (2008), 175501.
- [112] V. B.-Koutecký, P. Fantucci and J. Koutecký, Chem. Rev. **91** (1991), 1035.
- [113] I. Boustani, W. Pewestorf, P. Fantucci, V. B.-Koutecký and J. Koutecký, Phys. Rev. B **35** (1987), 9437.
- [114] P. Hohenberg and W. Kohn, Phys. Rev. **136** (1964), B864.
- [115] W. Kohn and L.J. Sham, Phys. Rev. **140** (1965), A1133.
- [116] E. Aprà, F. Baletto, R. Ferrando and A. Fortunelli, Phys. Rev. Lett. **93** (2004), 065502.
- [117] P. Nava, M. Sierka and R. Ahlrichs, Phys. Chem. Chem. Phys. **5** (2003), 3372.
- [118] D.M. Ceperley, Rev. Mod. Phys. **67** (1995), 279.
- [119] L. Mitás, J.C. Grossman, I. Stich and J. Tobik, Phys. Rev. Lett. **84** (2000), 1479.
- [120] J. Tersoff, Phys. Rev. B **37** (1988), 6991.
- [121] J. Tersoff, Phys. Rev. B **38** (1988), 9902.
- [122] J. Tersoff, Phys. Rev. Lett. **61** (1988), 2879.
- [123] J. Tersoff, Phys. Rev. B **39** (1989), 5566(R).
- [124] F.B. Mota, J.F. Justo and A. Fazzio, Phys. Rev. B **58** (1998), 8323.
- [125] F.B. Mota, J.F. Justo and A. Fazzio, J. Appl. Phys. **86** (1999), 1843.
- [126] D.W. Brenner, Phys. Rev. B **42** (1990), 9458.
- [127] S.J. Stuart, A.B. Tutein and J.A. Harrison, J. Chem. Phys. **122** (2000), 6472.
- [128] D.W. Brenner, O.A. Shenderova, J.A. Harrison, S.J. Stuart, B. Ni and S.B. Sinnott, J. Phys.: Condens. Matter **14** (2002), 783.
- [129] B. Ni, K.-H. Lee and S.B. Sinnott, J. Phys.: Condens. Matter **16** (2004), 7261.
- [130] K. Saitoh and H. Hayakawa, Prog. Theor. Phys **122** (2009), 1081.
- [131] K. Saitoh and H. Hayakawa, Phys. Rev. B **81** (2010), 115447.
- [132] K. Saitoh, A. Bodrova, H. Hayakawa, and N. V. Brilliantov, Phys. Rev. Lett. **105** (2010), 238001.
- [133] T. Ikeshoji, G. Torchet, M.-F. de Feraudy and K. Koga, Phys. Rev. E **63** (2001), 031101.
- [134] A. A. Radzig and B. M. Smirnov, *Parameters of Atoms and Atomic Ions* (Énergoatomizdat, Moscow, 1986).
- [135] D. D. Do and H. D. Do, Adsorpt. Sci. Technol. **21** (2003), 389.
- [136] A. Wongkoblap, D. D. Do and D. Nicholson, Phys. Chem. Chem. Phys. **10** (2008), 1106.

- [137] P. Deltour, J-L. Barrat and P. Jensen, *Phys. Rev. Lett.* **78** (1997), 4597.
- [138] L. J. Lewis, P. Jensen, N. Combe and J-L. Barrat, *Phys. Rev. B* **61** (2001), 16084.
- [139] K. Yasuoka and M. Matsumoto, *J. Chem. Phys.* **109** (1998), 8451.
- [140] J. J. Nicolas, K. E. Gubbins, W. B. Streett and D. J. Tildesly, *Mol. Phys.* **37** (1979), 1429.
- [141] W. Christen, U. Even, T. Raz and R. D. Levine, *J. Chem. Phys.* **108** (1998), 10262.
- [142] Q. Hou, M. Hou, L. Bardotti, B. Prével, P. Mélinon, and A. Perez, *Phys. Rev. B* **62** (2000), 2825.
- [143] M. P. Allen and D. J. Tildesley, *Computer Simulation of Liquids* (Clarendon press, Oxford, 1987).
- [144] S. V. Khare, N. C. Bartelt and T. L. Einstein, *Phys. Rev. Lett.* **75** (1995), 2148.
- [145] P. Nozières, *Solids Far From Equilibrium*, Chapter 1 (Cambridge University, Cambridge, England, 1992).
- [146] A. Pimpinelli and J. Villain, *Physics of Crystal Growth* (Cambridge University Press, Cambridge, United Kingdom, 1998).
- [147] P.J. Steinhardt, D.R. Nelson and M. Ronchetti, *Phys. Rev. B* **28** (1983), 784.
- [148] D. Cheng and D. Cao, *Chem. Phys. Lett.* **461** (2008), 71.
- [149] M.Á. Gracia-Pinilla, E.P. Tijerina, J.A. García, C. Fernández-Navarro, A. Tlahuice-Flores, S. Mejía-Rosales, J.M. Montejano-Carrizales and M. José-Yacamán, *J. Phys. Chem. C* **112** (2008), 13492.
- [150] E. V. Pugina, G. V. Kornich and G. Betz, *Phys. Solid State* **49** (2007), 580.
- [151] N. Inui, K. Mochiji, and K. Moritani, *Nanotechnology* **19** (2008), 505501.
- [152] A. A. Radzig and B. M. Smirnov, *Parameters of Atoms and Atomic Ions* (Énergoatomizdat, Moscow, 1986).
- [153] D. D. Do and H. D. Do, *Adsorpt. Sci. Technol.* **21** (2003), 389.
- [154] A. Wongkoblap, D. D. Do, and D. Nicholson, *Phys. Chem. Chem. Phys.* **10** (2008), 1106.
- [155] V. B. Shenoy, C. D. Reddy, A. Ramasubramaniam, and Y. W. Zhang, *Phys. Rev. Lett.* **101** (2008), 245501.
- [156] C. D. Reddy, A. Ramasubramaniam, V. B. Shenoy, and Y. W. Zhang, *Appl. Phys. Lett.* **94** (2009), 101904.
- [157] K. Yasuoka and M. Matsumoto, *J. Chem. Phys.* **109** (1998), 8451.
- [158] L. D. Landau and E. M. Lifshitz, *Theory of Elasticity* 3rd ed (Oxford, New York, 1986).
- [159] S. Timoshenko and S. W. Krieger, *Theory of Plates and Shells* 2nd ed. (McGraw-Hill, New York, 1959).
- [160] H. Kuninaka and H. Hayakawa, *J. Phys. Soc. Japan* **75** (2006), 074001.
- [161] H. Kuninaka and H. Hayakawa, *Prog. Theor. Phys. Suppl.* **178** (2009), 157.

- [162] H. S. Carslaw and J. C. Jaeger, *Conduction of Heat in Solids* 2nd ed (Oxford University Press, Amen House, London E. C. 4, 1959).
- [163] V. L. Berdichevsky, *Variational Principles of Continuum Mechanics* vol 1 (Springer Heidelberg Dordrecht London New York, 2009).
- [164] K. F. Riley, M. P. Hobson, and S. J. Bence, *Mathematical Methods for Physics and Engineering* 3rd ed (Cambridge University Press, The Edinburgh Building, Cambridge CB2 2RU, UK, 2006).
- [165] A. W. Leissa, *J. Sound and Vibration* **31** (1973), 257.
- [166] P. S. Frederiksen, *J. Sound and Vibration* **186** (1995), 743.
- [167] T. Schwager, V. Becker, and T. Pöschel, *Eur. Phys. J. E* **27** (2008), 107.
- [168] L. Labous, A.D. Rosato, and R.N. Dave, *Phys. Rev. E* **56** (1997), 5717.
- [169] C.M. Sorace, M.Y. Louge, M.D. Crozier and V.H.C. Law, *Mech. Res. Commun.* **36** (2009), 364.
- [170] L. D. Landau and E. M. Lifshitz, *Mechanics* (Oxford University Press, Oxford, 1965).
- [171] A.A. Kantak, C.M. Hrenya and R.H. Davis, *Phys. Fluids* **21** (2009), 023301.
- [172] C.M. Donahue, C. M. Hrenya and R. H. Davis, *Phys. Rev. Lett.* **105** (2010), 034501.
- [173] H.C. Hamaker, *Physica* **10** (1937), 1058.